



**HAL**  
open science

## Controlling the Cathodic Potential of KVPO<sub>4</sub>F through Oxygen Substitution

Romain Wernert, Long Nguyen, Emmanuel Petit, Paula Sanz Camacho, Antonella Iadecola, Alessandro Longo, François Fauth, Lorenzo Stievano, Laure Monconduit, Dany Carlier, et al.

► **To cite this version:**

Romain Wernert, Long Nguyen, Emmanuel Petit, Paula Sanz Camacho, Antonella Iadecola, et al.. Controlling the Cathodic Potential of KVPO<sub>4</sub>F through Oxygen Substitution. *Chemistry of Materials*, 2022, 34 (10), pp.4523-4535. 10.1021/acs.chemmater.2c00295 . hal-03690171

**HAL Id: hal-03690171**

**<https://cnrs.hal.science/hal-03690171>**

Submitted on 9 Jun 2022

**HAL** is a multi-disciplinary open access archive for the deposit and dissemination of scientific research documents, whether they are published or not. The documents may come from teaching and research institutions in France or abroad, or from public or private research centers.

L'archive ouverte pluridisciplinaire **HAL**, est destinée au dépôt et à la diffusion de documents scientifiques de niveau recherche, publiés ou non, émanant des établissements d'enseignement et de recherche français ou étrangers, des laboratoires publics ou privés.

# Controlling the Cathodic Potential of KVPO<sub>4</sub>F through Oxygen Substitution

Romain Wernert<sup>a,b,c</sup>, Long H.B. Nguyen<sup>a,c</sup>, Emmanuel Petit<sup>a,c</sup>, Paula Sanz Camacho<sup>a</sup>, Antonella Iadecola<sup>c</sup>, Alessandro Longo<sup>d,e</sup>, François Fauth<sup>f</sup>, Lorenzo Stievano<sup>b,c,g</sup>, Laure Monconduit<sup>b,c,g</sup>, Dany Carlier<sup>a,c,g</sup>, Laurence Croguennec<sup>a,c,g,\*</sup>

## AUTHOR ADDRESS

<sup>a</sup> Univ. Bordeaux, CNRS, Bordeaux INP, ICMCB, UMR 5026, F-33600 Pessac, France

<sup>b</sup> ICGM, Univ. Montpellier, CNRS, ENSCM, Montpellier, France

<sup>c</sup> RS2E, Réseau sur le Stockage Electrochimique de l'Énergie, FR CNRS 3459, Amiens F-80039 Cedex 1, France

<sup>d</sup> European Synchrotron Radiation Facility, 71, Avenue des Martyrs, Grenoble, F-38000, France

<sup>e</sup> Istituto per lo Studio dei Materiali Nanostrutturati (ISMN)-CNR, UOS Palermo via Ugo La Malfa 153 90146, Italy

<sup>f</sup> CELLS-ALBA synchrotron, E-08290, Cerdanyola del Vallès, Barcelona, Spain

<sup>g</sup> ALISTORE-ERI European Research Institute, FR CNRS 3104, F-80039 Amiens Cedex 1, France

\* Email: Laurence.Croguennec@icmcb.cnrs.fr

---

**ABSTRACT:** Exploring and tailoring new high energy density positive electrode materials is still a challenge for alkali-ion batteries. In this work we synthesized the mixed anion phases KVPO<sub>4</sub>F<sub>1-y</sub>O<sub>y</sub> (y = 0, 0.25, 0.5, 0.75, 1) and determined their crystallographic and electronic structures by combining synchrotron X-ray diffraction, X-ray absorption spectroscopy at vanadium K edge and <sup>31</sup>P MAS-NMR coupled with density functional theory calculations. These experiments confirmed the substitution of F<sup>-</sup> for O<sup>2-</sup> anions occurs as a solid solution across the whole composition domain. The local environments of vanadium ions are complex and diverse since the *cis* and *trans* octahedra undergo different distortions in presence of a vanadyl bond. The simultaneous existence of ionic V<sup>III</sup>-F bonds and covalent (V<sup>IV</sup>=O)<sup>2+</sup> vanadyl type entities is strongly affecting the electrochemical properties and potassium deinsertion/insertion mechanisms upon cycling. Ultimately, KVPO<sub>4</sub>F<sub>0.5</sub>O<sub>0.5</sub> appears as a promising positive electrode material due to its high capacity (105 mAh·g<sup>-1</sup>), working potential (4.2 V vs K<sup>+/K</sup>) and sloping electrochemical curve.

---

## ■ INTRODUCTION

K-ion batteries (KIBs) have been developed as future candidates for large scale and low cost energy storage thanks to the high abundance of potassium, the low electrochemical potential of K<sup>+/K</sup> and the possible use of graphite as negative electrode.<sup>1,2</sup> Among all the positive electrode materials for KIBs, potassium vanadium phosphate fluoride (KVPO<sub>4</sub>F) and oxide (KVOPO<sub>4</sub>) are the most promising ones.<sup>3,4</sup> These materials possess a theoretical capacity of 131 mAh·g<sup>-1</sup> and average voltage of 4.3 V vs K<sup>+/K</sup>, corresponding to a theoretical energy density of 560 Wh·kg<sup>-1</sup>, which is comparable to commercial LiFePO<sub>4</sub>-based Li-ion batteries.

KVPO<sub>4</sub>F and KVOPO<sub>4</sub> crystallize in the KTiOPO<sub>4</sub> (KTP) type structure (**Figure 1**) and can be described by the general formula KVPO<sub>4</sub>X (X = O, F).<sup>3,5</sup> The structure is built from corrugated chains made of corner-sharing VO<sub>4</sub>X<sub>2</sub> octahedra connected together by phosphate groups. Two different octahedral sites exist for vanadium, where the two anionic sites X in VO<sub>4</sub>X<sub>2</sub> octahedra alternate the *cis* and *trans* positions (**Figure 1**). In KV<sup>III</sup>PO<sub>4</sub>F, the octahedra along the chains are connected through fluorine anions, whereas in KV<sup>IV</sup>OPO<sub>4</sub>, they are connected through oxygen anions involved in highly covalent vanadyl-type {V=O}<sup>2+</sup> bonds. Potassium ions are also localized on two distinct sites with eight- and nine-fold coordination for K1 and K2 sites, respectively. Both sites are alternating along a helical diffusion channel that is collinear to the [001] direction. This KTP type structure is considered to be one of the most inductive with a record high redox potential of 3.6 V vs K<sup>+/K</sup> for the Ti<sup>IV</sup>/Ti<sup>III</sup> redox couple in KTiPO<sub>4</sub>.<sup>6,7</sup>

Many recent studies have shown that the anionic stoichiometry in vanadium phosphate materials, such as LiVPO<sub>4</sub>F<sub>1-y</sub>O<sub>y</sub> and Na<sub>3</sub>V<sub>2</sub>(PO<sub>4</sub>)<sub>2</sub>F<sub>3-2y</sub>O<sub>2y</sub> (0 ≤ y ≤ 1), has a great impact on their structure and electrochemical behaviour.<sup>8-16</sup> In the very first studies of KVPO<sub>4</sub>F, some discrepancies were found concerning the cell parameters reported for this composition.<sup>3,4</sup> Kim *et al.* later reported the importance of controlling the fluorine stoichiometry and proposed that the inconsistency observed in the literature was due to mixed F<sup>-</sup>/O<sup>2-</sup> anionic compositions.<sup>17</sup> These authors have indeed compared KVPO<sub>4</sub>F to a partially substituted composition, KVPO<sub>4</sub>F<sub>0.64</sub>O<sub>0.36</sub>, and revealed a discharge capacity lowered by 15 mAh·g<sup>-1</sup> and a smoother voltage curve for the latter. Nevertheless, it remains unclear

whether a solid solution for  $\text{KVPO}_4\text{F}_{1-y}\text{O}_y$  can exist in the whole range of  $0 \leq y \leq 1$ . Furthermore, the effects of oxygen substitution on the structural and electrochemical properties of  $\text{KVPO}_4\text{F}$  in batteries have not been fully explored yet.

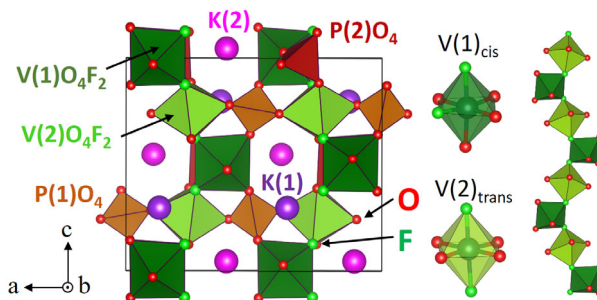


**Figure 1:** Crystal structure of  $\text{KVPO}_4\text{F}$ , built from undulating chains alternating  $\text{V}(1)\text{O}_4\text{F}_2$  and  $\text{V}(2)\text{O}_4\text{F}_2$  octahedra held together by phosphate tetrahedra. The chains are running along the  $[011]$  and  $[0-11]$  directions. The  $\text{VO}_4\text{F}_2$  octahedra, where the F ligands occupy the *cis* and *trans* positions are depicted as dark and light green, respectively.

To obtain an insightful understanding on the effects of fluorine-oxygen substitution in the  $\text{KVOPO}_4$ – $\text{KVPO}_4\text{F}$  system, a series of mixed anionic compositions  $\text{KVPO}_4\text{F}_{1-y}\text{O}_y$  ( $y = 0, 0.25, 0.5, 0.75, 1$ ) was synthesized and their “composition–structure–properties” relationship was investigated in detail. Here, we will provide a thorough description of the short and long range structures of  $\text{KVPO}_4\text{F}_{1-y}\text{O}_y$  in the whole compositional range, including the characterization of the distribution of vanadyl-type environments and the evolution of the electrochemical properties and performance in potassium batteries.

#### EXPERIMENTAL AND THEORETICAL APPROACH

**Material synthesis.** The  $\text{KVPO}_4\text{F}_{1-y}\text{O}_y$  ( $y = 0, 0.25, 0.5, 0.75, 1$ ) samples were synthesized by solid state reaction of  $\text{KF}$  (Alfa Aesar),  $\text{K}_2\text{CO}_3$  (Sigma-Aldrich, 99%),  $\text{VPO}_4$  and  $\text{VOPO}_4$  powders. The synthesis procedure for the two vanadium precursors,  $\text{VPO}_4$  and  $\text{VOPO}_4$ , consisted in first mixing  $\text{NH}_4\text{H}_2\text{PO}_4$  (98 % Sigma-Aldrich) and  $\text{V}_2\text{O}_5$  (99.6 %, Sigma-Aldrich). The mixture of powders was then heated at  $800^\circ\text{C}$  for 10 hours under  $\text{Ar}/\text{H}_2$  atmosphere to obtain  $\text{VPO}_4$ , which in turn was oxidized in air at  $750^\circ\text{C}$  for 5 hours to form  $\text{VOPO}_4$ . The quantities of  $\text{V}^{\text{III}}\text{PO}_4$  and  $\text{V}^{\text{V}}\text{OPO}_4$  were balanced so that the average oxidation state of vanadium in  $\text{KVPO}_4\text{F}_{1-y}\text{O}_y$  was equal to  $(3+y)$ . The precursors were weighted in an argon-filled glovebox with a 3 wt.% excess of  $\text{KF}$  to compensate the sticking and the loss of the material during the 45 minutes ball milling process. After mixing, the materials were pelletized (diameter 13 mm, 5t), and placed in a gold crucible. For  $y = 0.25, 0.5, 0.75$ , the thermal treatment was performed under argon atmosphere at  $650^\circ\text{C}$  for 6 hours. For  $\text{KVOPO}_4$ , a higher calcination temperature of  $750^\circ\text{C}$  was required. For  $\text{KVPO}_4\text{F}$  ( $y = 0$ ), drastic precautions were taken to avoid any partial oxidation by oxygen traces: the pellet was thus placed in a sealed gold tube under argon ( $< 0.1$  ppm  $\text{H}_2\text{O}/\text{O}_2$ ) and calcination was performed at  $650^\circ\text{C}$  for 6 hours. A continuous colour transition from green to brown going through violet is observed when moving from  $\text{KVPO}_4\text{F}$  to  $\text{KVOPO}_4$  (Figure S1).

**Scanning electron microscopy (SEM)** pictures of the powders were taken with a JEOL JSM 6700F field emission gun microscope with accelerating voltage of 15 kV. The materials were coated with 2 nm Pt to ensure charge drain.

**Fourier transformed infrared spectroscopy (FTIR)** data was acquired with a Bruker Equinox 55 spectrometer with a  $4\text{ cm}^{-1}$  resolution in the  $400\text{--}4000\text{ cm}^{-1}$  range. The samples were diluted in dried KBr.

**Synchrotron X-Ray powder diffraction (SXRD)** was performed at  $\lambda = 0.61908\text{ \AA}$  on BL04-MSPD beamline of ALBA synchrotron (Barcelona, Spain). Data was collected with the position sensitive detector MYTHEN, in Debye-Scherrer geometry, in the  $1^\circ$  to  $80^\circ$   $2\theta$  range with effective bin step of  $0.006^\circ$ . The diffractograms were refined with the JANA2006 program using a semi-rigid body method.<sup>18</sup> The P–O bond length was constrained to  $1.545 \pm 0.025\text{ \AA}$  and the atomic displacement parameters were refined together for i) the two phosphorus sites, ii) the eight oxygen sites belonging to phosphate groups, and iii) the two bridging sites X(1) and X(2) ( $X = \text{O}, \text{F}$ ). The compound  $\text{KVPO}_4\text{F}_{0.5}\text{O}_{0.5}$  was refined with anisotropic displacement parameters for X and V sites. In the case of partially substituted materials, the X(1) and X(2) sites were refined as fully occupied by fluorine since  $\text{F}^-$  and  $\text{O}^{2-}$  both have the electron configuration of  $[\text{He}] 2s^2 2p^6$ , thus possessing similar X-ray scattering factors. The standard uncertainties were corrected by the Bérar-Lelann factors<sup>19</sup> with values ranging from 3 to 5. The K sites splitting reported in some previous works<sup>3,17</sup> was neglected since it was not observed in the Fourier difference maps. Crystal structures were visualized with VESTA.<sup>20</sup>

**X-ray absorption spectroscopy (XAS)** was performed in transmission mode at the vanadium K-edge (5465 eV) at ROCK beamline<sup>21</sup> of Synchrotron SOLEIL (Saint-Aubin, France). A vanadium foil was used as the reference for energy calibration. The quick-EXAFS monochromator Si (111) was set at an oscillating frequency of 2 Hz. The samples were prepared by pelletizing a mixture of active

material (5.5 mg) and cellulose (35 mg) to form a 13 mm diameter disk with  $4.1 \text{ mg}\cdot\text{cm}^{-2}$  mass loading (active material). For each sample, 1200 quick-XAS data were averaged over 10 minutes acquisition time. Data treatment was carried out using the DEMETER software package.<sup>22</sup> EXAFS oscillations were  $k^2$  weighted and sine window ( $dk = 0$ ) was applied from 3.75 to  $12.2 \text{ \AA}^{-1}$  for the forward Fourier transform. Fitting was performed in the R range from 1 to  $2.15 \text{ \AA}$  with a sine window ( $dR = 0$ ) as well for the backward Fourier transform. The EXAFS parameters  $S_0^2$  was set to 1 and  $E_0$  was defined by the edge position at absorbance of 0.8 as already reported for similar XAS study.<sup>9</sup>

**X-ray Raman spectroscopy (XRS)** data were collected at the ID20 beamline of the ESRF (Grenoble, France). The pink beam from four U26 undulators was monochromatized to an incident energy of 9 683.7 eV, using a cryogenically cooled Si(111) monochromator and focused to a spot size of approximately  $30 \mu\text{m} \times 30 \mu\text{m}$  ( $V \times H$ ) at the sample position using a mirror system in Kirkpatrick-Baez geometry. XRS is an inelastic X-ray process, in which a high energy X-ray photon excites a core electron to an unoccupied state. The process is, in principle, analogous to X-ray Absorption (XAS), but the energy transfer to the outgoing photon plays the role of the X-ray photon energy absorbed in XAS. The large solid angle spectrometer at ID20 was used to collect XRS data with 36 spherically bent Si(660) crystal analysers. The data were treated with the XRStools program package as described elsewhere.<sup>23</sup> The sample was placed into the beam to have a  $10^\circ$  grazing incident beam. All XRS measurements were collected at room temperature. Full range scans were measured from 510 to 580 eV with a 1 eV step size. After acquisition of the broad scan, several detail scans of specific edges were collected with a 0.2 eV (fresh samples) or 0.7 eV (reduced samples) step by scanning the incident beam energy to record energy losses in the vicinity of the V  $L_{2,3}$ -edge and O K-edge (520-590 eV). Acquisition scans lasted around 6-8 h per sample. All scans were checked for consistency before averaging over them. The overall energy resolution of the XRS spectra was 0.7 eV as estimated from the full width at half maximum (FWHM) of elastic scattering from a piece of adhesive tape.

**<sup>31</sup>P solid-state nuclear magnetic resonance (NMR) spectroscopy** was performed using a Bruker Avance III 100 MHz spectrometer, equipped with a 2.4 T wide-bore magnet, leading to a Larmor frequency of 40.6 MHz for <sup>31</sup>P. 2.5 mm diameter rotors were filled with  $\approx 15$  mg of material and the magic-angle spinning (MAS) frequency was 30 kHz. A Hahn echo sequence was applied with a  $1.4 \mu\text{s}$   $90^\circ$  pulse and relaxation time of 0.2 s. Chemical shifts were referenced relative to an aqueous  $\text{H}_3\text{PO}_4$  85% (Sigma-Aldrich) solution at 0 ppm.

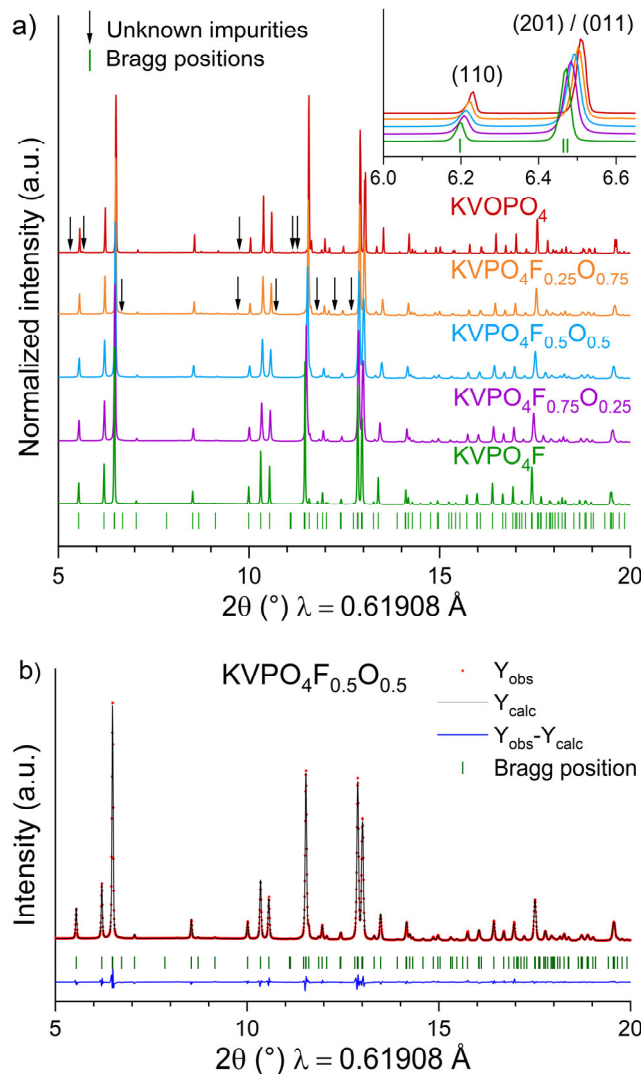
**Density functional theory calculations.** First-principles calculations were performed within the density functional theory (DFT) framework, and the calculations using the projector-augmented wave (PAW) method<sup>24,25</sup> were computed with the Vienna *Ab initio* Simulation Package (VASP) code<sup>24,26-29</sup>. The structural relaxation and total energy calculation were performed using the generalized gradient approximation (GGA) with the Perdew-Burke-Ernzerhof (PBE) exchange-correlation functional<sup>30</sup>. The self-interaction error of strongly correlated  $3d$  electrons was corrected using the rotationally invariant Dudarev method.<sup>31</sup> Different effective Hubbard corrections were tested for vanadium  $3d$ -electrons,  $U_{\text{eff}} (U - J) = 0.0, 3.0, 4.0, \text{ and } 5.0$  eV. All calculations were spin-polarized with ferromagnetic ordering, and performed with a plane-wave cutoff energy of 600 eV and a  $k$ -grid of  $4 \times 4 \times 4$ . The SXRD refined structures of  $\text{KVPO}_4\text{F}$  and  $\text{KVPO}_4\text{O}$  were used as inputs for the structural relaxation step.

The Fermi contact shifts were obtained from the computed isotropic hyperfine coupling parameters, as discussed in our previous works.<sup>32-35</sup> The nuclear gyromagnetic ratios ( $\text{MHz}\cdot\text{T}^{-1}$ ) of the nuclei involved in the calculations were 11.215 (<sup>51</sup>V), 17.2538 (<sup>31</sup>P), 1.987 (<sup>39</sup>K), 40.078 (<sup>19</sup>F), and 5.775 (<sup>17</sup>O). The Curie-Weiss temperature of  $\text{KVPO}_4$  ( $\theta_{\text{CW}} = 16$  K) was taken from the literature<sup>36</sup>, as well as the molar magnetic susceptibility ( $1.76 \mu_{\text{B}}$ ) and were consecutively used for the Fermi contact shift calculations. For  $\text{KVPO}_4\text{F}$ , magnetic susceptibility measurement was performed in zero field cooling conditions and the applied field was set to 5000 Oe. The measurement yielded  $\mu_{\text{eff}} = 2.68 \mu_{\text{B}}$  and  $\theta_{\text{CW}} = 3.5$  K. The temperature (T), at which the Fermi contact shifts were calculated, was chosen to be 320 K, which is the approximate temperature inside the rotor using a spinning frequency of 30 kHz. The 3D charge density and electronic spin density distribution maps were visualized utilizing VESTA software<sup>20</sup>.

**Battery preparation.** Electrodes were prepared using the tape casting method. 80 wt.% of active material were mixed together with 10 wt.% Super P carbon black and 10 wt.% PVDF (Fluka,  $M_w = 534\,000 \text{ g}\cdot\text{mol}^{-1}$ ) in N-methyl-2-pyrrolidone (Sigma Aldrich, 99% anhydrous) for 1 hour. The slurry was then casted on a  $20 \mu\text{m}$  aluminium foil and dried overnight at  $80^\circ\text{C}$ . 16 mm diameter disks were cut and pressed under 5 tons. The porosity of the electrodes ranged between 30-32 % and the loading of active material was  $2.8\text{-}3.2 \text{ mg}\cdot\text{cm}^{-2}$ . After overnight drying of the electrodes at  $10^{-2}$  mbar and  $80^\circ\text{C}$ , the cells were assembled in an argon filled glovebox, using 316L stainless steel coin cell (CR2032 type) components. Two disks of Viledon fiber mat (Freudenberg) were used as the separator, 50  $\mu\text{L}$  of  $\text{KPF}_6$  (0.8 M) in EC:DEC (volumetric ratio 1:1) electrolyte were added ( $\text{KPF}_6$ , Sigma-Aldrich,  $\geq 99\%$ ; EC, Sigma-Aldrich, anhydrous, 99%; DEC, Sigma-Aldrich, anhydrous,  $\geq 99\%$ ). Potassium metal (99.95%, Alfa Aesar) was used as counter-electrode. Standard galvanostatic electrochemical tests were performed at a C/20 nominal current (corresponding to 1 mol of  $\text{K}^+$  deintercalated in 20 hours). Galvanostatic intermittent titration technique (GITT) was performed at C/50 during the second cycle, in discharge only with steps of 15 minutes ( $\Delta x = 0.005$ ) and relaxation time until  $dE/dt$  is inferior to  $1 \text{ mV}\cdot\text{h}^{-1}$ . The electrochemical curves of the second cycle were offset to start at  $x=1$  in order to ignore the large irreversible capacity occurring during the first cycle.

▪ RESULTS AND DISCUSSION

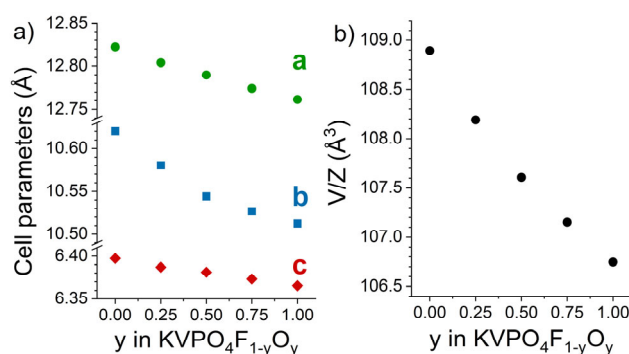
**Structural characterization.** The SXRD patterns of  $\text{KVPO}_4\text{F}_{1-y}\text{O}_y$  ( $y = 0, 0.25, 0.5, 0.75, 1$ ) samples are displayed in **Figure 2a**. All of them exhibit the same characteristic peaks, with however noticeable shifts attributed to changes in the cell parameters of  $\text{KVPO}_4\text{F}_{1-y}\text{O}_y$  as a function of the oxygen content. Crystallites size was retrieved from Scherrer formula. The lowest value of 200 nm was obtained for the  $\text{KVPO}_4\text{F}_{0.5}\text{O}_{0.5}$  material (**Figure S2**) whereas the end member compounds have crystallite sizes close to 1  $\mu\text{m}$  for  $\text{KVPO}_4\text{F}$  or even bigger for  $\text{KVOPO}_4$ . The morphology of each composition was observed with SEM (**Figure S3**) which unveils more divided morphology for the intermediate compositions. The presence of impurities, not detected by laboratory X-ray diffraction, are revealed by SXRD for the oxygen-rich compositions,  $\text{KVOPO}_4$  and  $\text{KVPO}_4\text{F}_{0.25}\text{O}_{0.75}$ , but both remain unmatched to any known compound. Nevertheless, considering that only small amounts of impurities is detected, these samples are considered as pure enough for the structural determination by Rietveld refinement. The structure of all  $\text{KVPO}_4\text{F}_{1-y}\text{O}_y$  samples can be described in the orthorhombic system with the  $Pna2_1$  space group ( $n^\circ 33$ ), and no superstructure peaks are detected in any of the materials.



**Figure 2:** a) SXRD pattern of the  $\text{KVPO}_4\text{F}_{1-y}\text{O}_y$  materials. b) Rietveld refinement of the SXRD pattern of  $\text{KVPO}_4\text{F}_{0.5}\text{O}_{0.5}$ . Reliability factors are  $\chi^2 = 10.2$ ,  $R_p = 3.7\%$ ,  $R_{wp} = 4.8\%$ .

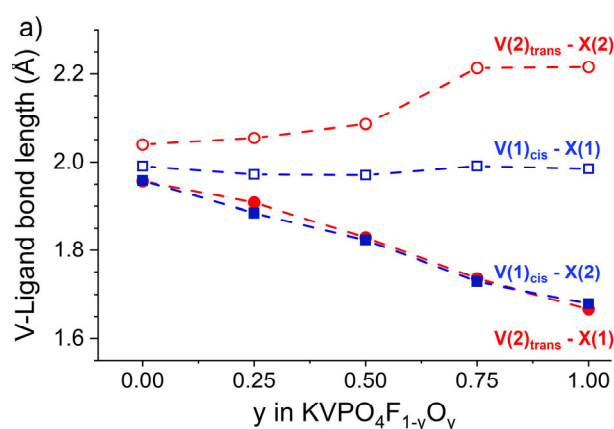
**Figure 2b** shows the results of the Rietveld refinement performed for  $\text{KVPO}_4\text{F}_{0.5}\text{O}_{0.5}$ . The experimental pattern can be simulated with a single phase, meaning that there is no segregation into the end member compounds. Similar fit quality was achieved for all five materials, and the corresponding crystallographic information is given in **Figures S4-7** and **Tables S1-6**. A monotonic decrease of

the cell parameters and the normalized unit cell volumes ( $V/Z$ ) is observed when moving from  $\text{KVPO}_4\text{F}$  to  $\text{KVOPO}_4$  (**Figure 3**). Indeed, the replacement of  $\text{F}^-$  by  $\text{O}^{2-}$  anions leads to the formation of the short and covalent vanadyl bonds ( $\text{V}^{\text{IV}}=\text{O}$ ), and hence smaller cell parameters. FTIR spectroscopy (**Figure S8**) confirmed the formation of vanadyl bonds with increasing oxygen content as one can see in the absorption features at  $850$  and  $900\text{ cm}^{-1}$  typical of  $\text{V}=\text{O}$  stretching modes.<sup>37</sup> We suggest the two signals can be attributed to the vanadyl bonds present either on the  $\text{V}(1)$  or  $\text{V}(2)$  sites, where the *cis* and *trans* configurations slightly modulates the vibration frequencies. Moreover, the absence of  $\text{O}-\text{H}$  stretching modes ( $3500\text{ cm}^{-1}$ ) confirms that the fluorine-rich compounds are not hydroxyl-substituted.



**Figure 3:** Variation of a) the cell parameters and b) the unit cell volume per formula unit as function of the oxygen content in  $\text{KVPO}_4\text{F}_{1-y}\text{O}_y$ . The standard uncertainties are smaller than symbol size.

**Figure 4a** shows the evolution of the interatomic distances between the two vanadium cations and the bridging anions  $\text{X}$  ( $\text{X} = \text{O}, \text{F}$ ) as function of the oxygen content resulting from the Rietveld refinements of the SXRD patterns. In  $\text{KVPO}_4\text{F}$ , all bond lengths are close to  $2\text{ Å}$ , in good agreement with the typical quasi-symmetric octahedral environments for  $\text{V}^{\text{III}}$ . However when fluorine is substituted by oxygen, shorter and covalent vanadyl bonds are formed simultaneously for both  $\text{V}(1)_{\text{cis}}$  and  $\text{V}(2)_{\text{trans}}$ , ultimately reaching the value of  $1.67\text{ Å}$  for the fully substituted end member  $\text{KVOPO}_4$ , as expected for a vanadyl bond.<sup>38</sup> At the same time, the antagonist  $\text{V}(2)_{\text{trans}}-\text{X}(2)$  bond increases gradually on the  $\text{V}(2)_{\text{trans}}$  site. The difference in the distortion of the local environment is visualized in **Figure 4b**. The  $\text{V}(2)_{\text{trans}}$  local environment can be described by the  $[1+4+1]$  coordination, meaning that the  $\text{V}_{\text{trans}}\text{O}_4\text{X}_2$  octahedron can be decomposed into one short  $\text{V}-\text{X}$  bond, four intermediate  $\text{V}-\text{O}$  bonds in a square plane, and one long  $\text{V}-\text{X}$  bond opposite to the short one. On the other hand,  $\text{V}(1)_{\text{cis}}$  distorts in an unusual way, adopting a  $[1+5]$  configuration (one short  $\text{V}-\text{X}$  bond, five intermediate  $\text{V}-\text{X}/\text{O}$  bonds). Contrary to Tavorite  $\text{LiVOPO}_4$ , the shortening due to  $\text{V}=\text{O}$  bonds in KTP-structure does not always induce an elongation in its opposite position. In the case of partially substituted materials, each bond length  $\text{V}-\text{X}$  determined from the Rietveld refinement of the XRD patterns is the average of different chemical configurations. This is further supported by the evolution of the atomic displacement parameters determined for  $\text{V}(1)_{\text{cis}}$  and  $\text{V}(2)_{\text{trans}}$ , as shown in **Figure S9**. In this specific case, the increase of  $B_{\text{iso}}$  of  $\text{V}$  and  $\text{K}$  atoms is more due to the distribution of slightly different local environments around these atoms than to a thermal effect. The refinement of  $\text{KVPO}_4\text{F}_{0.5}\text{O}_{0.5}$  was performed with anisotropic displacement parameters. **Figure S10** displays the  $\text{VO}_4\text{X}_2$  chain with the atomic displacement ellipsoid for  $\text{V}$  and  $\text{X}$  sites. It can be seen that the ellipsoids of  $\text{V}$  are mostly spherical, and that the ones of  $\text{X}$  sites are very elongated. This behaviour highlights the fact that the changing in bond length is mostly driven by repositioning of the  $\text{X}$  ligands rather than displacement of  $\text{V}$  within its octahedron. The bond valence sum (BVS) is also calculated and shown to be in very good agreement with the expected average oxidation state for vanadium (**Figure 4b** and **Figure S11**).



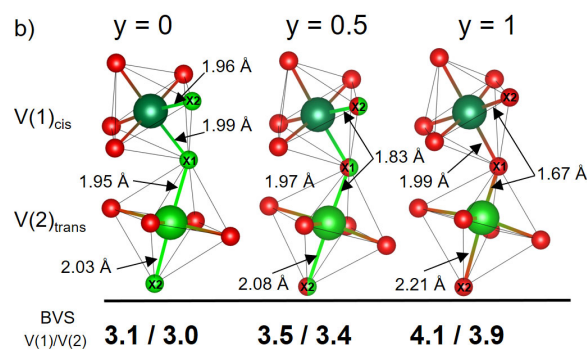


**Figure 4:** a) Evolution of the V–X bond lengths as function of the oxygen content in KVPO<sub>4</sub>F<sub>1-y</sub>O<sub>y</sub>, X being the bridging ligand anions (F<sup>-</sup> or O<sup>2-</sup>) between two successive octahedra along the distorted chains building the KTP type framework; the dotted lines are used for eye guidance. b) Description of the V(1)<sub>cis</sub> and V(2)<sub>trans</sub> octahedra in KVPO<sub>4</sub>F ( $y = 0$ ), KVPO<sub>4</sub>F<sub>0.5</sub>O<sub>0.5</sub> ( $y = 0.5$ ) and KVOPO<sub>4</sub> ( $y = 1$ ). The bond lengths are determined by the Rietveld refinement and the charge on each vanadium is calculated by BVS.

In order to finely determine vanadium's oxidation state and local environment, V K-edge XAS was performed on the whole series of KVPO<sub>4</sub>F<sub>1-y</sub>O<sub>y</sub> samples. The X-ray Absorption Near Edge Structure (XANES) region is presented in **Figure 5a**. Na<sub>3</sub>V<sup>III</sup><sub>2</sub>(PO<sub>4</sub>)<sub>3</sub> and NaV<sup>IV</sup>OPO<sub>4</sub> are used as references to determine vanadium oxidation state from the position of the absorption edges. The edge position of KVPO<sub>4</sub>F<sub>1-y</sub>O<sub>y</sub> compositions lies in the range between Na<sub>3</sub>V<sub>2</sub>(PO<sub>4</sub>)<sub>3</sub> and NaVOPO<sub>4</sub>, thus evidencing an average intermediate oxidation state between +3 and +4. The edge position shifts linearly to higher energy with the increase of the oxygen content in KVPO<sub>4</sub>F<sub>1-y</sub>O<sub>y</sub>, (**Figure 5**), as expected from a nuclear charge screening effect less important for V<sup>IV</sup> than for V<sup>III</sup>. Moreover, the pre-edge intensity increases significantly upon oxygen substitution. Indeed, the pre-edge region is very sensitive to V oxidation state and its local geometry.<sup>39-41</sup> It features the transitions from vanadium 1s core states to its empty 3d states which are only allowed in the case of non-centrosymmetric environments, due to metal 3d-4p hybridization. Hence the pre-edge intensity is directly proportional to the amount of V sites distorted by the formation of vanadyl bonds. In particular, two weak signals typical of V<sup>III</sup> environments are observed for KVPO<sub>4</sub>F at 5467.8 and 5469.4 eV. Besides, the pre-edge of KVOPO<sub>4</sub> is characterized by a single intense peak (at 5469.4 eV). For partially substituted materials, the absolute and integrated intensity of the pre-edge evolves linearly with the expected amount of V=O entities (**Figure S12**). Moreover, all the spectra of partially substituted materials could be obtained as linear combination of the spectra of the two end members KVPO<sub>4</sub>F and KVOPO<sub>4</sub>. As shown in **Table 1**, a very good agreement with the theoretical values is obtained, confirming the excellent control of the stoichiometry and revealing similar local structures in the end member compounds and in the partially substituted phases. XRS was also performed to probe vanadium L<sub>2,3</sub>-edges as shown in **Figure 5b**. Because the L<sub>2,3</sub>-edges lie in the soft X-ray energy range, they are usually measured with surface-sensitive techniques (e.g., total electron or fluorescence yields). With XRS, a high-energy X-ray technique, a large volume of the sample is probed, resulting in an L<sub>2,3</sub>-edges signal representing the bulk of the sample. According to multiplet theory, the energy position and the intensity ratio of the peaks are diagnostic of the electronic states of the atom involved, which in this case is vanadium. The experimental spectra were compared to calculated ones performed with the Crispy computer program. The software allows the calculation of core-level spectra using the semi-empirical multiplet approaches implemented in the Quanty script language for regular metal polyhedra,<sup>42,43</sup> and confirms that the experimental peaks at 517 and 518 eV are indicative of the presence of V<sup>3+</sup> and V<sup>4+</sup>. This allows us to exclude the presence of previously reported V<sup>2+</sup> from the bulk of KVPO<sub>4</sub>F as it would imply bulk V<sup>4+</sup> for charge compensation and hence considerably broaden the signals.<sup>44</sup>

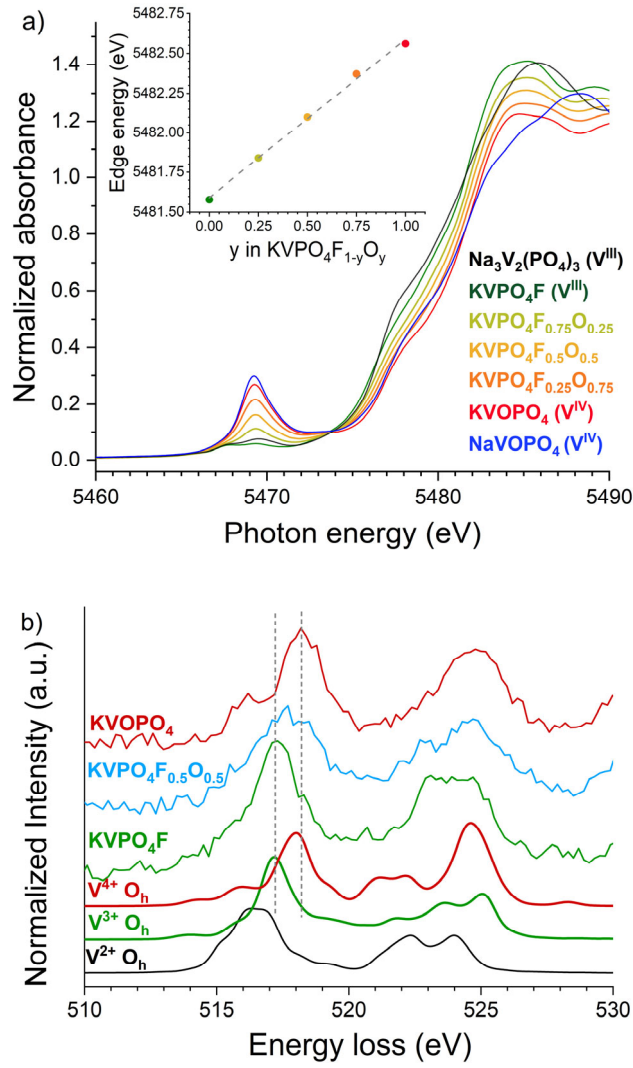


**Figure 5:** a) V K-edge XANES spectra of  $\text{KVPO}_4\text{F}_y\text{O}_{1-y}$ , along with references. Inset shows the position of the edge at absorbance 1 as function of the composition. b) XRS V  $L_{2,3}$ -edges and corresponding multiplet simulations.

**Table 1:** Results from the linear combination fitting of the XAS spectra of intermediate  $\text{KVPO}_4\text{F}_{1-y}\text{O}_y$  by those of the end members  $\text{KVPO}_4\text{F}$  and  $\text{KVOPO}_4$

	$\text{KVPO}_4\text{F}$	$\text{KVOPO}_4$	R factor
	(%)	(%)	
$\text{KVPO}_4\text{F}$	100	0	-
$\text{KVPO}_4\text{F}_{0.75}\text{O}_{0.25}$	72	28	$9 \cdot 10^{-4}$
$\text{KVPO}_4\text{F}_{0.50}\text{O}_{0.50}$	50	50	$1 \cdot 10^{-4}$
$\text{KVPO}_4\text{F}_{0.25}\text{O}_{0.75}$	23	77	$8 \cdot 10^{-4}$
$\text{KVOPO}_4$	0	100	-

Subsequently, the analysis of the Extended X-ray Absorption Fine Structure (EXAFS) oscillations was performed to retrieve quantitative information on the  $\text{V}(\text{O},\text{F})_6$  local structure. The octahedral environments determined previously by SXRD for the two types of vanadium,  $\text{V}(1)_{\text{cis}}$  and  $\text{V}(2)_{\text{trans}}$ , were used as starting models to perform the EXAFS fit. Since both are contributing equally (50/50) to the EXAFS signal, we simplified the possible scattering paths by considering only three different types of bonds, namely regular  $\text{V}-\text{O}/\text{F}$  bonds, short  $\text{V}=\text{O}$  vanadyl, and long  $\text{V}-\text{O}$ , each of them being associated to a coordination number  $N$  fixed accordingly with

its statistical probability. A similar approach was already successfully applied for  $\text{LiVPO}_4\text{F}_{1-y}\text{O}_y$  materials.<sup>45</sup> However, as the number of long V—O bond ranges from  $N=0.5$  for  $\text{KVPO}_4\text{O}$  to  $N=0$  in the regular  $\text{KVPO}_4\text{F}$  compound, we finally considered it as a regular V—O bond to avoid parameters correlation leading to unphysical V—O distance values. The structural fitting model thus consisted in:

- Short V=O vanadyl bonds that exist for both V(1) and V(2) in oxidized samples, with a probability of  $y$ .
- Regular V—O/F bonds that are around 2 Å and are weighted by  $6-y$

Finally, a different Debye-Waller factor was used to take into account the different covalency of the V=O bonds as compared to V—O as well as the possible distribution in V—O/F bond lengths.

The first peak of the magnitude of the Fourier Transform corresponds to the  $\text{V}(\text{O},\text{F})_6$  local environment and it is well described with the aforementioned structural model, as shown in **Figure S13**. The resulting bond lengths and Debye-Waller factors are compared in **Table 2**. For the two end members, the bond lengths obtained from EXAFS analysis are perfectly consistent with those determined by XRD, as in both cases the local environments of vanadium atoms correspond to the average description of the vanadium octahedral sites. On the contrary, for all the intermediate compositions showing a statistical distribution of O and F as bridging anions between successive octahedra along the chains, the V=O bond determined from EXAFS fitting is effectively shorter (1.65 Å), as expected, than those reported (1.82 Å) in  $\text{KVPO}_4\text{F}_{0.5}\text{O}_{0.5}$  by XRD Rietveld refinement. Indeed, that latter is the weighted average between the ionic bond V—F and the covalent bond V=O. For oxygenated compounds, the Debye-Waller factors corresponding to the V=O bonds are significantly lower than those of V—O/F bonds. This result reflects both the strong covalency together with the directionality of the oxometal vanadyl bond, which determine the higher stiffness of the V=O bond compared to the V—O/F bond, as well as the larger distribution of bond distances for the latter contribution. In summary, the description of the local environments of vanadium atoms in the substituted phases is very consistent with the formation of a solid solution between  $\text{KVOPO}_4$  and  $\text{KVPO}_4\text{F}$ .

**Table 2:** Refined EXAFS parameters corresponding to the local structure of  $\text{V}(\text{O},\text{F})_6$  octahedra.

Material	Bond	N	R (Å)	Debye-Waller Factor ( $10^{-3} \text{Å}^2$ )	EXAFS agreement factor (%)	Average bond length from XRD (Å)
$\text{KVPO}_4\text{F}$	V—O/F	6	2.01 (1)	5.1 (3)	0.3	1.98 (3)
$\text{KVPO}_4\text{F}_{0.75}\text{O}_{0.25}$	V—O/F	5.75	2.01(1)	5.8 (3)	0.3	1.99 (3)
	V=O	0.25	1.64(2)	2 (1)		1.89 (1)
$\text{KVPO}_4\text{F}_{0.50}\text{O}_{0.50}$	V—O/F	5.5	2.01 (1)	6.2 (5)	0.3	1.99 (3)
	V=O	0.5	1.65 (1)	2 (1)		1.82 (1)
$\text{KVPO}_4\text{F}_{0.25}\text{O}_{0.75}$	V—O/F	5.25	2.01 (1)	7.4 (5)	0.2	2.01 (4)
	V=O	0.75	1.65 (1)	2 (1)		1.73(1)
$\text{KVOPO}_4$	V—O	5	2.01 (1)	8.5 (8)	0.2	2.02 (7)
	V=O	1	1.65 (1)	2 (1)		1.67 (1)

**Solid-state nuclear magnetic resonance spectroscopy.**  $^{31}\text{P}$  MAS-NMR spectroscopy was performed to obtain insightful information on the atomic local environments in  $\text{KVPO}_4\text{F}_{1-y}\text{O}_y$  compositions. **Figure 6** shows  $^{31}\text{P}$  MAS-NMR spectra recorded for the complete series of compounds. The spectrum of  $\text{KVPO}_4\text{F}$  is characterized by two isotropic signals, at 5800 and 4450 ppm. In the case of  $\text{KVOPO}_4$ , two isotropic signals located at much lower shifts of 1975 and 1000 ppm are observed. Qualitatively, each peak can be assigned to a specific phosphorus local environment. In the case of  $\text{KVPO}_4\text{F}$ , we previously confirmed an oxidation state of +III for all V ions, corresponding to the  $d^2$  electronic configuration. Likewise, the oxidation state of +IV in  $\text{KVOPO}_4$  corresponds to the  $d^1$  configuration. Hence, we could expect a lower spin transfer from V to  $^{31}\text{P}$  in the case of  $\text{KVOPO}_4$ . The Rietveld refinement reveal there exist P(1) and P(2) sites in KTP-structure, the two resonances observed in  $\text{KVPO}_4\text{F}$  or  $\text{KVOPO}_4$  may be assigned to these two sites. Despite the fact that KTP structure presents as many P(1) and P(2) sites, a noticeable difference in the intensity of integrated signals can be noticed (19% and 81% of the total integrated signal for  $\text{KVOPO}_4$ , **Figure S14**). To rationalize this phenomenon, we measured the spin-spin ( $T_2$ ) relaxation constant for  $\text{KVOPO}_4$  under MAS by varying the Hahn echo sequence refocalization delay and then integrating the peak intensities. **Figure S15** shows an exponential decrease in the intensity of the  $^{31}\text{P}$  MAS-NMR resonances as function of the refocalization delay. Based on those measurements,  $T_2$  relaxation times (under MAS) for signals are extracted. The  $T_2$  relaxation time of the most shifted signal (2000 ppm) is much shorter than that of the 1000 ppm signal,  $40 \pm 1 \mu\text{s}$  vs  $154 \pm 2 \mu\text{s}$ , respectively. Since the refocusing delay (one rotor period synchronized Hahn echo sequence) used for the MAS spectra in **Figure 6** is  $33.33 \mu\text{s}$ , which is close to the  $T_2$  relaxation time of the most shifted signal, whose signal intensity is much weaker compared to the second signal. Similar observations were previously reported for  $\text{LiFePO}_4 \cdot \text{OH}$  and  $\text{LiFePO}_4 \cdot \text{H}_2\text{O}$  phases.<sup>32</sup>

For partially substituted compounds, the spectra are characterized by wide signals in the intermediate range between the end-members. Four different regions are identified around 1500, 2500, 3000 and 3500 ppm with variable intensities depending on the O content. This further assess the existence of a solid solution of  $\text{F}/\text{O}^{2-}$  ions in  $\text{KVPO}_4\text{F}_{1-y}\text{O}_y$ .

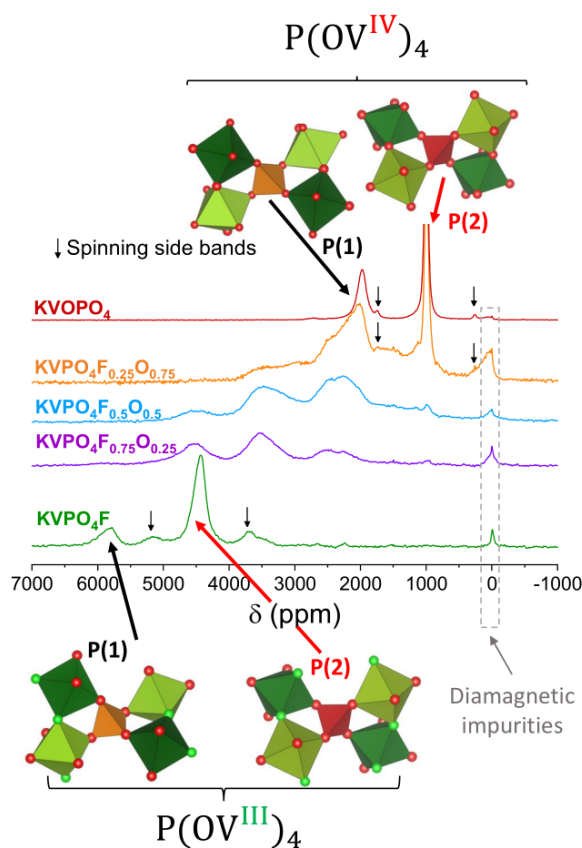


**Figure 6:** Solid state  $^{31}\text{P}$  MAS NMR spectra collected for the  $\text{KVPO}_4\text{F}_{1-y}\text{O}_y$  materials.

Consecutively, DFT calculations were performed in order to assign the signals to specific chemical environments as well as to explain the spin transfer mechanism between vanadium ions and phosphorus sites. The SXR D refined structure of  $\text{KVPO}_4\text{F}$  was used as input model. The cell parameters of  $\text{KVPO}_4\text{F}$  optimized by GGA and GGA+U approaches are given in **Table S7**. Both GGA and GGA+U approaches are able to reproduce the cell parameters of  $\text{KVPO}_4\text{F}$  within the error bar of 1–2%. The V–O/F distances calculated by GGA and GGA+U show that all  $\text{V}^{\text{III}}$  ions in  $\text{KVPO}_4\text{F}$  reside in a symmetric octahedral site (**Table S8**), which is entirely in agreement with the structure determined by SXR D and EXAFS. Fermi contact shifts are calculated for the two P sites in  $\text{KVPO}_4\text{F}$ , using the experimental Curie-Weiss temperature and Curie constant for  $\text{KVPO}_4\text{F}$  (**Figure S16**). Whatever the used method, GGA or GGA+U with different  $U_{\text{eff}}$  values, the shift calculated for P(1) is larger than the one calculated for P(2) (**Table 3**) allowing us to assign the observed signals as depicted in **Figure 6**, e.g. 5800 ppm signal to P(1) and 4450 ppm to P(2). Furthermore, the absolute value of the calculated  $^{31}\text{P}$  Fermi contact shift depends strongly on the  $U_{\text{eff}}$  applied in the calculation: when a higher  $U_{\text{eff}}$  value is used, the  $^{31}\text{P}$  signal is less shifted. This tendency has also been observed in our previous studies.<sup>32–34,46,47</sup> Higher  $U_{\text{eff}}$  value tends to localize the unpaired electrons on V sites, reducing the magnitude of the electron spin–nucleus coupling, and thus the  $^{31}\text{P}$  NMR shifts. For  $U_{\text{eff}} = 4$  eV, the experimental  $^{31}\text{P}$  NMR shifts of  $\text{KVPO}_4\text{F}$  are well reproduced (**Table 3**), indicating the electron spin distribution and the magnitude of the nuclear spin–spin coupling in the structure are appropriately described. This  $U_{\text{eff}}$  value will further be used to analyze the electronic structure and spin transfer mechanism.

**Table 3:** Experimental Fermi contact shifts (in ppm) of  $^{31}\text{P}$  nuclei in  $\text{KVPO}_4\text{F}$  compared to those computed by the VASP code with different  $U_{\text{eff}}$  values.

	GGA	GGA+3eV	GGA+4eV	GGA+5eV	Experimental data
P(1)	11500	6840	5830	5040	5800
P(2)	8180	5470	4680	4020	4450

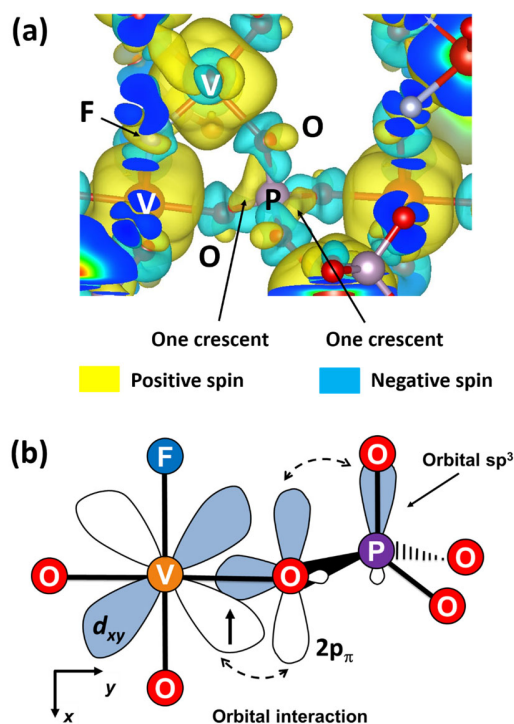


**Figure 7:** (a) 3D spin density map showing the electron spin-transfer mechanism from a  $V^{III}$  ion to a neighbouring phosphorus ( $5 \times 10^{-4}$  electron $\cdot\text{\AA}^{-2}$  isosurface value). The map was calculated on the  $KVPO_4F$  structure relaxed with the GGA+U method ( $U_{\text{eff}} = 4$  eV). The positive and negative electron spins are represented in yellow and blue, respectively. The electron spin density surrounding P sites in  $KVPO_4F$  structure looks like two crescents located on two opposite sides of the P. (b) Schematic representation of the spin transfer mechanism from  $V^{III}$  to P by the  $d_{xy}(V^{III}) - p_{\pi}(O) - sp^3(P)$  orbital hybridization. The x and y axes are chosen arbitrarily and independent of the crystallographic axes.

In order to gain insightful information on the spin-transfer mechanism between  $V^{III}$  and  $^{31}\text{P}$  nuclei, the 3D electron spin density maps are plotted. The yellow color in **Figure 7a** indicates the presence of the positive spin (“spin-up”) electrons of  $V^{III}$ . These electrons reside mainly in the proximity of vanadium sites, and the homogeneous spin distribution indicates a partial occupation of the  $t_{2g}$  orbitals. One of the orbitals in the degenerated  $t_{2g}$  level, i.e.,  $d_{xy}$ , has such an orientation with the O 2p orbital and the P hybridized  $sp^3$  orbital, that it leads to the  $d_{xy}(V^{III}) - p_{\pi}(O) - sp^3(P)$  interaction (**Figure 7b**). The electron spins on  $V^{III}$  are delocalized over P sites, leading to a strong Fermi contact interaction. Phosphorus in  $KVPO_4F$  receives the spin transfer from four surrounding  $V^{III}$ . Nevertheless, the unique orientation of  $VO_4F_2$  polyhedra results in a particular form of the spin density on P sites, which looks like two crescents located on two opposite sides of the P (**Figure 7a**). The spin-transfer mechanism and the form of the spin density are identical for P(1) and P(2) sites in  $KVPO_4F$ ; there is, however, a slight difference in the  $V^{III}$ –P distances observed for the two sites. The experimental SXRD data shows that  $V^{III}$ –P(2) distances ( $2 \times 3.23$  Å, 3.30 Å, and 3.33 Å) are slightly longer than  $V^{III}$ –P(1) distances (3.21 Å,  $2 \times 3.23$  Å, and 3.27 Å), thus a lower orbital overlap is expected. The electron spin density transferred on the P(2) nucleus is then lower than the one transferred on P(1), and the corresponding NMR signal is less shifted.

Similar to  $KVPO_4F$ , the experimental cell parameters of  $KVOPO_4$  are well reproduced by structural relaxation with the GGA and GGA+U methods at different  $U_{\text{eff}}$  values (**Table S9**). Nevertheless, the V–O distances reproduced with  $U_{\text{eff}} = 0$  eV show a broader dispersion in the values compared to the experimental data or other  $U_{\text{eff}}$  values (**Table S10**). The 3D spin density map reveals a difference in the degeneracy of the 3d levels of  $V^{IV}$  obtained with different  $U_{\text{eff}}$  values. In the GGA approach, the electron spin of  $V^{IV}$  is located on all  $t_{2g}$  orbitals, indicating that  $d_{xy}$ ,  $d_{xz}$ , and  $d_{yz}$  levels are quasi-degenerated (**Figure 8a**). On the other hand, the electron spin only occupies the  $d_{xy}$  orbital in the GGA+U approach, implying that the lift of degeneracy of the  $t_{2g}$  orbitals (**Figure 8b**), which is a consequence of the presence of the short vanadyl bond.<sup>48</sup> This observation is entirely in agreement with our previous study showing the GGA+U approach is required to reproduce the electronic structure of  $V^{IV}$  in the Tavorite  $LiVOPO_4$ .<sup>34</sup> It will be thus further used here to compute the Fermi contact shifts on P(1) and P(2) (**Table 4**).

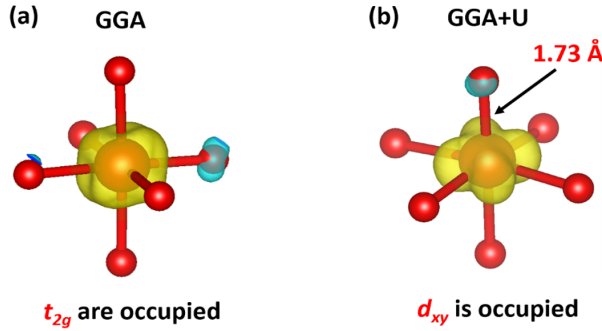


**Figure 8:** Spin distribution map surrounding a  $\text{VO}_6$  octahedron in  $\text{KVPO}_4\text{O}$  calculated by (a) GGA and (b) GGA+U method. An isosurface value of  $9 \times 10^{-3}$  electron $\cdot\text{\AA}^{-2}$  was used for these plots. The x and y axes used to define the name of the orbital are chosen arbitrarily.

As the GGA+U method gives a better description of the electronic structure of  $\text{V}^{\text{IV}}$  in  $\text{KVPO}_4$ , the Fermi contact shifts will thus be calculated from the nuclear spin–spin coupling constants obtained from GGA+U. The calculated Fermi contact shifts of P(1) and P(2) are very different (**Table 4**), indicating a significant difference in their local electronic structures, despite their similar geometry. The 3D spin distribution map reveals that P(1) in  $\text{KVPO}_4$  is surrounded by four  $\text{V}^{\text{IV}}$  and the four  $d_{xy}$  orbitals containing the electron spin are pointing towards the oxygens shared between  $\text{V}^{\text{IV}}$  and P (**Figure 9a**). Therefore, the  $d_{xy}(\text{V}^{\text{IV}}) - p_{\pi}(\text{O}) - sp^3(\text{P})$  orbital hybridization (**Figure 7a**) can occur, and the electron spin on  $\text{V}^{\text{IV}}$  is delocalized over P(1) sites, leading to a highly shifted  $^{31}\text{P}$  NMR signal. The electron spin-transfer mechanisms between vanadium ions and P(1) sites in  $\text{KVPO}_4\text{O}$  can be schematized similarly to the one that occurs in  $\text{KVPO}_4\text{F}$  (**Figure 9a** versus **Figure 7a**); nevertheless,  $\text{V}^{\text{III}}$  in  $\text{KVPO}_4\text{F}$  possesses two unpaired electrons while  $\text{V}^{\text{IV}}$  in  $\text{KVPO}_4$  only has one, hence the  $^{31}\text{P}$  NMR signal in  $\text{KVPO}_4\text{F}$  has a higher Fermi contact shift value. The P(2) site in  $\text{KVPO}_4$  is also surrounded by four  $\text{V}^{\text{IV}}$  ions; however, one  $d_{xy}$  orbital of the four neighbouring  $\text{V}^{\text{IV}}$  is perpendicular to the  $\text{V}-\text{O}_{\text{sharing}}$  bond, and the P(2) site receives the electron spin from three  $\text{V}^{\text{IV}}$  only (**Figure 9b**). In  $\text{KVPO}_4$ , the electron spin density on P(2) is therefore lower than P(1), and the  $^{31}\text{P}$  NMR signal arising from P(2) is less shifted.

**Table 4.** Experimental Fermi contact shifts (in ppm) of  $^{31}\text{P}$  nuclei in  $\text{KVPO}_4$  compared to those computed by the VASP code with different  $U_{\text{eff}}$  values.

	GGA	GGA+3eV	GGA+4eV	GGA+5eV	Experimental data
P(1)	2170	2950	2700	2490	1975
P(2)	1800	1600	1420	1370	1000

In  $\text{KVPO}_4\text{F}$ , the P(1) and P(2) local environments are  $\text{P}(\text{OV}^{\text{III}})_4$  with different distances and angles for P(1) and P(2). Upon O-substitution, the oxygen ions are distributed randomly over the O/F bridging anionic sites, leading to a random formation of  $\text{V}^{\text{IV}}$  and  $\text{V}^{\text{III}}$  sites. Besides  $\text{P}(\text{OV}^{\text{III}})_4$ , new phosphorus local environments are generated, including  $\text{P}(\text{OV}^{\text{III}})_3(\text{OV}^{\text{IV}})$ ,  $\text{P}(\text{OV}^{\text{III}})_2(\text{OV}^{\text{IV}})_2$ ,  $\text{P}(\text{OV}^{\text{III}})(\text{OV}^{\text{IV}})_3$ , and  $\text{P}(\text{OV}^{\text{IV}})_4$ . By considering the inequivalence of P(1) and P(2) on one hand, and V(1), V(2) on the other hand, one can expect eighteen different phosphorus local environments in  $\text{KVPO}_4\text{F}_{1-y}\text{O}_y$  ( $0 < y < 1$ ), but local modification of distances and angles can lead to even more possibilities. As we evidenced that for a given oxidation state of V ions, the shifts difference for the two P sites could be as large as 1350 ppm ( $\text{V}^{\text{III}}$ ) and considering that full oxidation shifts the P(1) and P(2) signals by approximately -3600 ppm (approximately -900 ppm per  $\text{V}^{4+}$  around P), the signal assignment of the experimental spectra of the intermediate  $\text{KVPO}_4\text{F}_{1-y}\text{O}_y$  phases is challenging and out of the scope of this study.

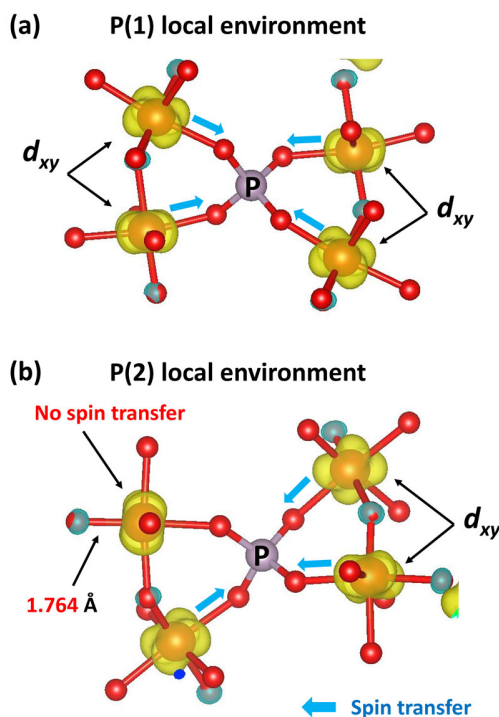


**Figure 9.** 3D spin density map, calculated on the  $\text{KVPO}_4\text{O}$  structure relaxed with the GGA+U method ( $U_{\text{eff}} = 5 \text{ eV}$ ), reveals the local environment and the electron spin transfer between  $\text{V}^{4+}$  and (a) P(1), and (b) P(2) sites. An isosurface value of  $2 \times 10^{-2} \text{ electron} \cdot \text{\AA}^{-2}$  was used for these plots. The x and y axes used to define the name of the orbital are chosen arbitrarily. The blue arrows indicate the spin transfer direction between  $\text{V}^{4+}$  and the shared oxygen atoms.

**Electrochemical properties.** The electrochemical behaviour of the mixed-anion compounds was evaluated in potassium metal half-cells and compared to those of the end members  $\text{KVPO}_4\text{F}$  and  $\text{KVOPO}_4$ . **Figure 10** presents the galvanostatic curves obtained for the second cycle at a rate of  $C/20$  (*i.e.*, exchange of  $1 \text{ e}^-$  or  $1 \text{ K}^+$  in 20 hours) and the corresponding derivative plots. Since the cell parameters after first discharge were found to be identical to the pristine compound for  $\text{KVPO}_4\text{F}$ , denoting fully reversible  $\text{K}^+$  insertion (**Figure S17**), the electrochemical curves of the second cycle were offset to start at  $x=1$  in order to ignore the large irreversible capacity occurring during the first cycle. The electrochemical activity of  $\text{KVPO}_4\text{F}$  is identical to that already reported in the literature, with three successive characteristic sloping domains in the 4 to 4.5 V vs.  $\text{K}^+/\text{K}$  voltage range and a very long plateau at 4.9 V with a total reversible capacity of  $105 \text{ mAh} \cdot \text{g}^{-1}$ .<sup>17</sup>

For the partially substituted compounds, the plateaus and the potential jump at 4.5 V tend to disappear. Indeed, the electrochemical signature of  $\text{KVPO}_4\text{F}_{0.5}\text{O}_{0.5}$  is completely sloping all over the composition range in potassium, except for a small plateau ( $\sim 0.1 \text{ K}^+$  wide) observed at the beginning of the charge. This supports the existence of a mixed anionic disorder between  $\text{F}^-$  and  $\text{O}^{2-}$  all along the octahedra chains, which creates a distribution of environments for K and V,  $\text{KO}_{7+2y}\text{F}_{2-2y}$  and  $(\text{V}^{\text{III}}_{1-y}\text{V}^{\text{IV}}_y)\text{O}_{4+2y}\text{F}_{2-2y}$ , which prevents the formation of  $\text{K}^+$  - vacancy, V charge orderings, and thus well-defined phase transitions. For all materials, the first cycle has a low coulombic efficiency limited to 60-70 % (**Figure S18**), which was already attributed to parasitic reactions involving electrolyte degradation and the formation of an electrode-electrolyte solid interphase.<sup>44</sup> The increase of the fluorine content in  $\text{KVPO}_4\text{F}_{1-y}\text{O}_y$  ( $y \leq 0.5$ ) goes along with an increase of the irreversible capacity in the first cycle. Indeed, as we are working with non-optimized K-containing electrolytes, electrolyte stability issues are more critical for these F-rich compositions reacting at high voltage.<sup>44</sup> The difference in the nature of the surface (fluoride phosphate versus oxyfluoride phosphate) could also play a role in catalysing electrolyte degradation, but this study which is in progress remains outside the scope of this paper.

For oxygen-rich compounds ( $y > 0.5$ ), a systematic capacity decrease is observed as a function of the oxygen content from  $105 \text{ mAh} \cdot \text{g}^{-1}$  for  $\text{KVPO}_4\text{F}_{0.5}\text{O}_{0.5}$  to only  $68 \text{ mAh} \cdot \text{g}^{-1}$  ( $0.5 \text{ K}^+$  exchanged) for  $\text{KVOPO}_4$ . The average redox potential between  $\text{K}_1\text{VPO}_4(\text{F},\text{O})$  and  $\text{K}_{0.5}\text{VPO}_4(\text{F},\text{O})$  was estimated by averaging the potential of all cathodic and anodic derivative peaks and thus neglecting kinetic contributions. It was found to be  $E(\text{V}^{4+/3+}) = 4.2 \text{ V}$  for  $\text{KVPO}_4\text{F}$  and  $E(\{\text{V}^{5+/4+}=\text{O}\}) = 4.35 \text{ V}$  for  $\text{KVOPO}_4$ . It is likely that the limited capacity of the most oxygenated materials arises from this higher redox potential, meaning a full  $\text{K}^+$  de-intercalation would occur above 5 V vs  $\text{K}^+/\text{K}$ .

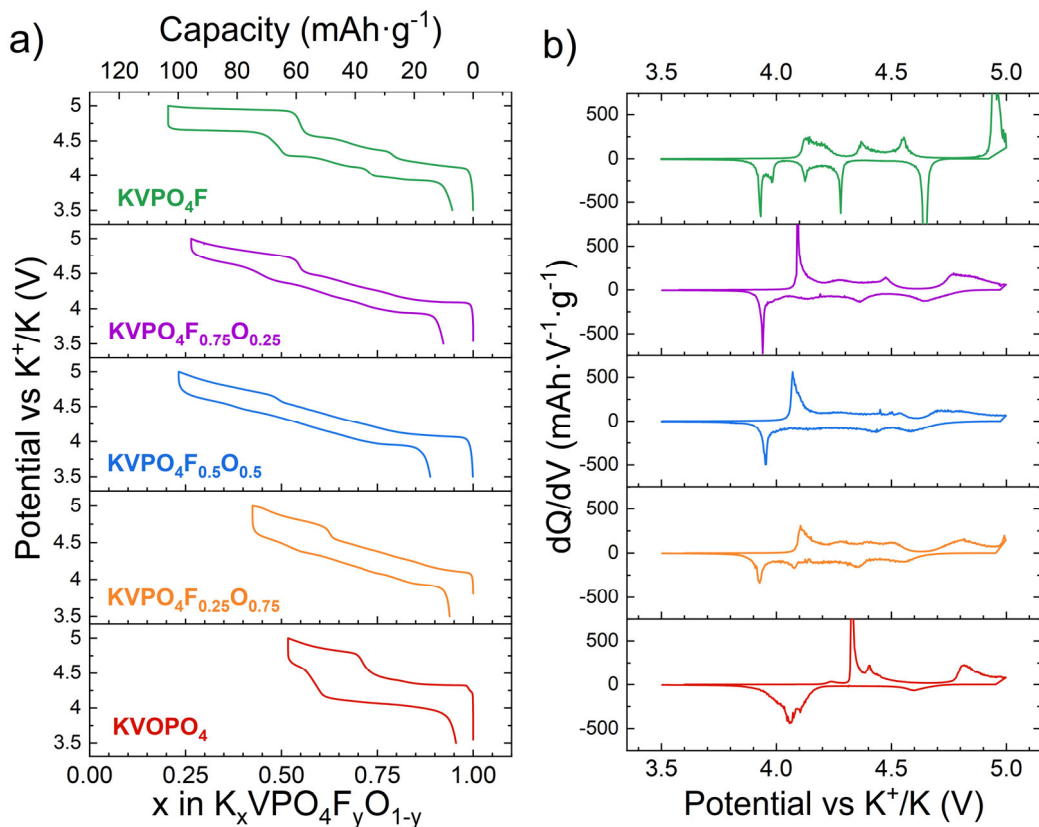


**Figure 10:** a) Galvanostatic curves (2<sup>nd</sup> cycle) obtained for all materials in K metal half-cells at C/20. b) Corresponding derivative curves.

The sloping electrochemical curve of  $\text{KVPO}_4\text{F}_{0.5}\text{O}_{0.5}$  in K metal half-cell associated with high capacity ( $105 \text{ mAh}\cdot\text{g}^{-1}$ ) makes it a very interesting material since its state of charge can be known just by measuring the rest potential (which is not the case for any biphasic insertion electrode material). For this particular compound, we performed GITT and measured the areal diffusion coefficient during discharge as shown in **Figure 11**. The rest thermodynamic potential follows a quasi linear curve with a slope of  $1.7 \text{ V}/\text{K}^+$  deintercalated, a very low value compared to potassium layered oxides,  $5.6 \text{ V}/\text{K}^+$  for  $\text{K}_x\text{MnO}_2$  for example<sup>16</sup> but still considerably higher than  $\text{LiVPO}_4\text{F}_{0.5}\text{O}_{0.5}$  ( $0.1 \text{ V}/\text{Li}^+$ ) and  $\text{Na}_3\text{V}_2(\text{PO}_4)_2\text{F}_3$  ( $0.25 \text{ V}/\text{Na}^+$ ) owing to the large ionic radii of K. The  $\text{K}_{0.5}\text{VPO}_4\text{F}_{0.5}\text{O}_{0.5}$  composition can be identified by the small voltage jump at 4.6 V in charge, which appears at lower  $\text{K}^+$  content in discharge due to high voltage parasitic reactions that lead to a competitive consumption of the electrons for the irreversible oxidation of the electrolyte and for  $\text{K}^+$  de-intercalation.

Three different domains can be distinguished from the electrochemical curve and trends in the diffusion coefficient:

- Domain (I) at the beginning of charge is characterized by a  $0.1 \text{ K}^+$  wide plateau.
- Domain (II) features a constant slope curve with a “diffusion coefficient” of  $\approx 10^{-9} \text{ cm}^6\cdot\text{s}^{-1}$  until the  $\text{K}_{0.5}\text{VPO}_4\text{F}_{0.5}\text{O}_{0.5}$  composition.
- Domain (III) still presents a solid solution type curve but with a drop by 1 order of magnitude of the diffusion coefficient. The origin of this phenomenon can be attributed to the fact that the site energy and activation barrier for migration are different for each potassium site, as calculated by Lian *et al.* in  $\text{KVOPO}_4$  but needs to be evidenced in further work for  $\text{KVPO}_4\text{F}$  and mixed anionic compositions  $\text{KVPO}_4\text{F}_{1-y}\text{O}_y$ .<sup>49</sup>

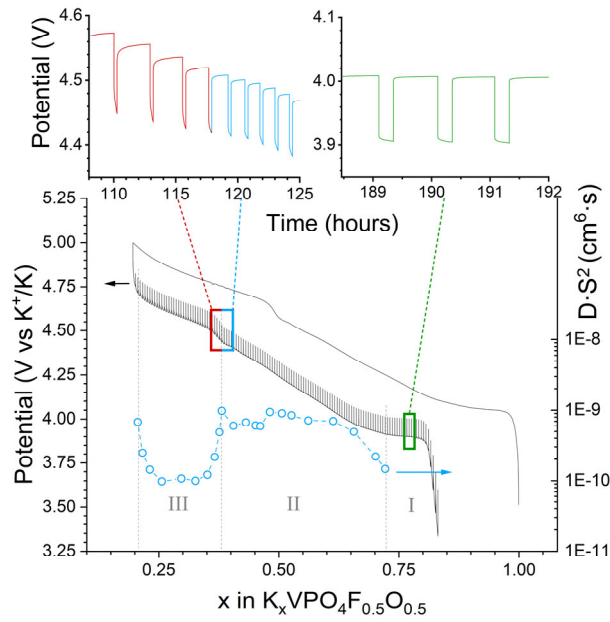


**Figure 11:** Continuous galvanostatic charge performed at a rate of  $C/50$  followed by a discharge performed in GITT conditions for  $\text{KVPO}_4\text{F}_{0.5}\text{O}_{0.5}$  (at a rate of  $C/50$ , with steps of 15 minutes ( $\Delta x = 0.005$ ) and relaxation time until the slope  $dE/dt$  is inferior to  $1 \text{ mV} \cdot \text{h}^{-1}$ ).

This study reveals intriguing behaviour of the redox potential as function of the chemical composition. The 230 mV increase from  $\text{KVPOF}$  to  $\text{KVOPO}_4$  is surprising when drawing the comparison between  $\text{KVPO}_4\text{F}_{1-y}\text{O}_y$  on one side and  $\text{LiVPO}_4\text{F}_{1-y}\text{O}_y$  and  $\text{Na}_3\text{V}_2(\text{PO}_4)_2\text{F}_{3-y}\text{O}_y$  on the other side. Indeed, for these two latter vanadium oxyfluoride phosphate compounds, the oxidation of  $\{\text{V}^{4+}=\text{O}\}$  to  $\{\text{V}^{5+}=\text{O}\}$  systematically lies at a lower potential than that of  $\text{V}^{3+}-\text{O}/\text{F}$  into  $\text{V}^{4+}-\text{O}/\text{F}$ . **Figure 12** summarizes the topology of  $\text{VO}_4\text{X}_2$  polyhedra, and their electrochemical potential referenced against the standard hydrogen electrode. One can see strong similarities in Tavorite and KTP-type structures due to the presence of infinite 1D chains, though the connectivity differs with only *trans* type octahedra in  $\text{LiVPO}_4\text{F}_{1-y}\text{O}_y$ . In fully oxygen substituted compounds, the V-V distance and V-X-V bond angles are nearly the same (contraction of 0.4%, slight opening of angles) as in the fluorine counterpart sample for the case of Tavorite and expands by 6.3% for  $\text{Na}_3\text{V}_2(\text{PO}_4)_2\text{FO}_2$  bioctahedra, and for both cases the electrochemical potential drops by 100 to 300 mV. However, when the V-V distances are approximately 3.55 Å in  $\text{KVPO}_4\text{F}$ , the inequivalent vanadyl distortions occurring for V(1) and V(2) in  $\text{KVOPO}_4$  leads to alternating short and long V-V distances of 3.33 Å and 3.62 Å, resembling to a Peierls distortion.

The comparison between the three systems,  $\text{LiVPO}_4\text{F}_{1-y}\text{O}_y$ ,  $\text{Na}_3\text{V}_2(\text{PO}_4)_2\text{F}_{3-y}\text{O}_y$ , and  $\text{KVPO}_4\text{F}_{1-y}\text{O}_y$ , shows that the relative electrochemical potential of fluoride phosphate and vanadyl phosphate material cannot be solely interpreted in terms of inductive effect of fluoride ion and that the crystal structure may actually be a more significant determining factor.

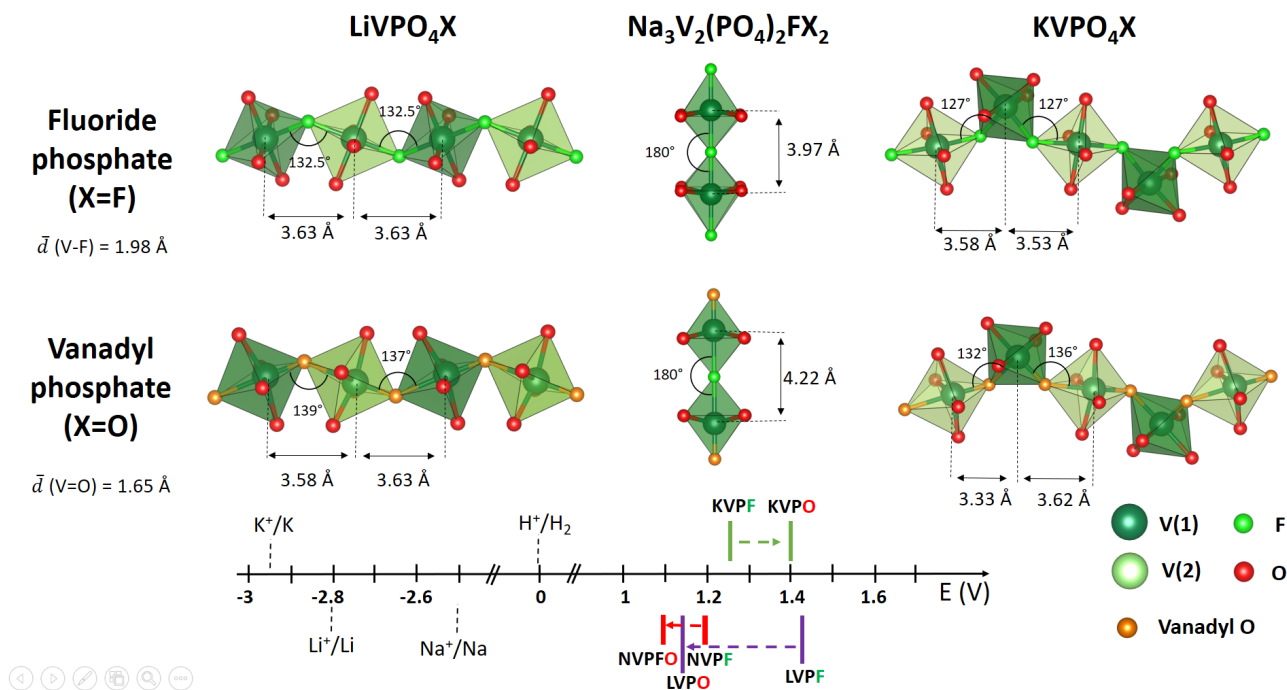


**Figure 12:** Top: topology of the vanadium polyhedra in tavorite type  $\text{LiVPO}_4\text{F}_{1-y}\text{O}_y$ ,  $\text{Na}_3\text{V}_2(\text{PO}_4)_2\text{F}_{3-y}\text{O}_y$  and KTP type  $\text{KVPO}_4\text{F}_{1-y}\text{O}_y$ . The V-X-V angles and V-V distances are depicted. Bottom: potential scale referenced versus  $\text{H}^+/\text{H}_2$ . The potentials of alkali metals are considered in EC:DEC solvent. For  $\text{Na}_3\text{V}_2(\text{PO}_4)_2\text{F}_3$  (NVPF) and  $\text{Na}_3\text{V}_2(\text{PO}_4)_2\text{FO}_2$  (NVPFO) only the first plateau is considered. For  $\text{KVPO}_4\text{F}$  and  $\text{KVOPO}_4$  the potential between  $\text{K}_1\text{VPO}_4(\text{F},\text{O})$  and  $\text{K}_{0.5}\text{VPO}_4(\text{F},\text{O})$  is considered.

## CONCLUSION

This work demonstrates the feasibility of finely controlling the anionic composition in the  $\text{KVPO}_4\text{F} - \text{KVOPO}_4$  system. First, we show that at the global long range (SXR) and local scale (EXAFS) the substituted phases form a solid solution of the two end members of the series. The  $\text{F}^-$  and  $\text{O}^{2-}$  ions are statistically distributed along the X sites and hence no local segregation of fluorine (or oxygen) rich environments is observed. This is further supported by the study of the electronic structure probed by  $^{31}\text{P}$  MAS NMR spectroscopy. The signals identified for the substituted materials are different from the ones of  $\text{KVOPO}_4$  and  $\text{KVPO}_4\text{F}$ , and we successfully identified the spin transfer path responsible for the observed paramagnetic signals. Finally, the electrochemical properties of the materials show a great diversity. The most disordered phase shows a large capacity ( $105 \text{ mAh} \cdot \text{g}^{-1}$ ) with a continuous sloping voltage profile. This behaviour is attributed to the anionic solid solution which multiplies the number of different local environments for potassium and vanadium ions and hence prevents alkali-vacancy orderings. The redox mechanisms involved during cycling, especially for mixed valence compounds, remains an open question together with the origin of the voltage increase between the fluoride and oxide members. Further investigations are being carried out to explain and understand the peculiarities of the KTP structure with respect to other phosphate (fluoride, oxide) materials.

## ASSOCIATED CONTENT

**Supplementary information.** Photograph of KVPO<sub>4</sub>F<sub>0.5</sub>O<sub>0.5</sub> powders, detailed crystallographic information and XRD refinements, SEM pictures, FTIR spectroscopy, complementary EXAFS, NMR, magnetic susceptibility and DFT data analysis.

Crystallographic Information Files (CIF) of KVPO<sub>4</sub>F, KVPO<sub>4</sub>F<sub>0.5</sub>O<sub>0.5</sub>, KVPO<sub>4</sub>F<sub>0.25</sub>O<sub>0.75</sub>, KVPO<sub>4</sub>.

## AUTHOR INFORMATION

### Corresponding Author

**Laurence Croguennec** – Univ. Bordeaux, CNRS, Bordeaux INP, ICMCB, UMR 5026, F-33600 Pessac, France; RS2E, Réseau sur le Stockage Electrochimique de l’Energie, FR CNRS 3459, Amiens F-80039 Cedex 1, France; ALISTORE-ERI European Research Institute, FR CNRS 3104, F-80039 Amiens Cedex 1, France; [orcid.org/0000-0002-3018-0992](https://orcid.org/0000-0002-3018-0992); Email: [Laurence.Croguennec@icmcb.cnrs.fr](mailto:Laurence.Croguennec@icmcb.cnrs.fr)

### Authors

**Romain Wernert** – Univ. Bordeaux, CNRS, Bordeaux INP, ICMCB, UMR 5026, F-33600 Pessac, France; ICGM, Univ. Montpellier, CNRS, ENSCM, Montpellier, France; RS2E, Réseau sur le Stockage Electrochimique de l’Energie, FR CNRS 3459, Amiens F-80039 Cedex 1, France; [orcid.org/0000-0002-5073-4008](https://orcid.org/0000-0002-5073-4008)

**Long H. B. Nguyen** – Univ. Bordeaux, CNRS, Bordeaux INP, ICMCB, UMR 5026, F-33600 Pessac, France; RS2E, Réseau sur le Stockage Electrochimique de l’Energie, FR CNRS 3459, Amiens F-80039 Cedex 1, France; [orcid.org/0000-0001-7823-1595](https://orcid.org/0000-0001-7823-1595)

**Emmanuel Petit** – Univ. Bordeaux, CNRS, Bordeaux INP, ICMCB, UMR 5026, F-33600 Pessac, France; RS2E, Réseau sur le Stockage Electrochimique de l’Energie, FR CNRS 3459, Amiens F-80039 Cedex 1, France;

**Paula Sanz Camacho** – Univ. Bordeaux, CNRS, Bordeaux INP, ICMCB, UMR 5026, F-33600 Pessac, France; [orcid.org/0000-0003-4898-8225](https://orcid.org/0000-0003-4898-8225)

**Antonella Iadecola** – RS2E, Réseau sur le Stockage Electrochimique de l’Energie, FR CNRS 3459, Amiens F-80039 Cedex 1, France; [orcid.org/0000-0002-9031-8455](https://orcid.org/0000-0002-9031-8455)

**Alessandro Longo** – European Synchrotron Radiation Facility, 71, Avenue des Martyrs, Grenoble, F-38000, France; Istituto per lo Studio dei Materiali Nanostrutturati (ISMN)-CNR, UOS Palermo via Ugo La Malfa 153 90146, Italy; [orcid.org/0000-0002-8819-2128](https://orcid.org/0000-0002-8819-2128)

**François Fauth** – CELLS-ALBA synchrotron, E-08290, Cerdanyola del Vallès, Barcelona, Spain; [orcid.org/0000-0001-9465-3106](https://orcid.org/0000-0001-9465-3106)

**Lorenzo Stievano** – ICGM, Univ. Montpellier, CNRS, ENSCM, Montpellier, France; RS2E, Réseau sur le Stockage Electrochimique de l’Energie, FR CNRS 3459, Amiens F-80039 Cedex 1, France; ALISTORE-ERI European Research Institute, FR CNRS 3104, F-80039 Amiens Cedex 1, France; [orcid.org/0000-0001-8548-0231](https://orcid.org/0000-0001-8548-0231)

**Laure Monconduit** – ICGM, Univ. Montpellier, CNRS, ENSCM, Montpellier, France; RS2E, Réseau sur le Stockage Electrochimique de l’Energie, FR CNRS 3459, Amiens F-80039 Cedex 1, France; ALISTORE-ERI European Research Institute, FR CNRS 3104, F-80039 Amiens Cedex 1, France; [orcid.org/0000-0003-3698-856X](https://orcid.org/0000-0003-3698-856X)

**Dany Carlier** – Univ. Bordeaux, CNRS, Bordeaux INP, ICMCB, UMR 5026, F-33600 Pessac, France; RS2E, Réseau sur le Stockage Electrochimique de l’Energie, FR CNRS 3459, Amiens F-80039 Cedex 1, France; ALISTORE-ERI European Research Institute, FR CNRS 3104, F-80039 Amiens Cedex 1, France; [orcid.org/0000-0002-5086-4363](https://orcid.org/0000-0002-5086-4363)

## ACKNOWLEDGMENTS

This work was part of the TROPIC project supported by Agence Nationale de la Recherche (ANR) under the grant ANR-19-CE05-0026. ANR is also acknowledged for funding the RS2E network through the STORE-EX Labex Project ANR-10-LABX-76-01. Synchrotron Soleil (France) is acknowledged for providing beamtime at the beamline ROCK (proposal #20191774) which also benefits from ANR grant as part of the “Investissements d’Avenir” program ANR-10-EQPX-45. MSPD staff of ALBA is acknowledged for the supply of inhouse beamtime (proposal number 2021035158). The Mésocentre de Calcul Intensif Aquitain (MCIA) and the modeling center of ISM are acknowledged for computing facilities. The authors also thank C. Denage, Ph. Legros and J. Olchowka, for their general technical support, SEM images, and FTIR spectroscopy measurements, respectively. M. Guignard is acknowledged for her help during magnetic susceptibility measurement.

## REFERENCES

- (1) Hosaka, T.; Kubota, K.; Hameed, A. S.; Komaba, S. Research Development on K-Ion Batteries. *Chem. Rev.* **2020**, *acs.chemrev.9b00463*. <https://doi.org/10.1021/acs.chemrev.9b00463>.
- (2) Kim, H.; Ji, H.; Wang, J.; Ceder, G. Next-Generation Cathode Materials for Non-Aqueous Potassium-Ion Batteries. *Trends in Chemistry* **2019**, *1* (7), 682–692. <https://doi.org/10.1016/j.trechm.2019.04.007>.
- (3) Fedotov, S. S.; Khasanova, N. R.; Samarin, A. Sh.; Drozhzhin, O. A.; Batuk, D.; Karakulina, O. M.; Hadermann, J.; Abakumov, A. M.; Antipov, E. V. AVPO<sub>4</sub>F (A = Li, K): A 4 V Cathode Material for High-Power Rechargeable Batteries. *Chem. Mater.* **2016**, *28* (2), 411–415. <https://doi.org/10.1021/acs.chemmater.5b04065>.
- (4) Chihara, K.; Katogi, A.; Kubota, K.; Komaba, S. KVPO<sub>4</sub>F and KVOPO<sub>4</sub> toward 4 Volt-Class Potassium-Ion Batteries. *Chem. Commun.* **2017**, *53* (37), 5208–5211. <https://doi.org/10.1039/C6CC10280H>.
- (5) Benhamada, L.; Grandin, A.; Borel, M. M.; Leclaire, A.; Raveau, B. KVPO<sub>5</sub>, an Intersecting Tunnel Structure Closely Related to the Hexagonal Tungsten Bronze. *Acta Crystallogr C Cryst Struct Commun* **1991**, *47* (6), 1138–1141. <https://doi.org/10.1107/S0108270190014044>.

- (6) Fedotov, S. S.; Luchinin, N. D.; Aksyonov, D. A.; Morozov, A. V.; Ryazantsev, S. V.; Gaboardi, M.; Plaisier, J. R.; Stevenson, K. J.; Abakumov, A. M.; Antipov, E. V. Titanium-Based Potassium-Ion Battery Positive Electrode with Extraordinarily High Redox Potential. *Nat Commun* **2020**, *11* (1), 1484. <https://doi.org/10.1038/s41467-020-15244-6>.
- (7) Fedotov, S. S.; Samarin, A. S.; Antipov, E. V. KTiOPO<sub>4</sub>-Structured Electrode Materials for Metal-Ion Batteries: A Review. *Journal of Power Sources* **2020**, *480*, 228840. <https://doi.org/10.1016/j.jpowsour.2020.228840>.
- (8) Broux, T.; Bamine, T.; Fauth, F.; Simonelli, L.; Olszewski, W.; Marini, C.; Ménétrier, M.; Carlier, D.; Masquelier, C.; Croguennec, L. Strong Impact of the Oxygen Content in Na<sub>3</sub>V<sub>2</sub>(PO<sub>4</sub>)<sub>2</sub>F<sub>3-2x</sub>O<sub>x</sub> (0 ≤ x ≤ 0.5) on Its Structural and Electrochemical Properties. *Chem. Mater.* **2016**, *28* (21), 7683–7692. <https://doi.org/10.1021/acs.chemmater.6b02659>.
- (9) Boivin, E.; David, R.; Chotard, J.-N.; Bamine, T.; Iadecola, A.; Bourgeois, L.; Suard, E.; Fauth, F.; Carlier, D.; Masquelier, C.; Croguennec, L. LiVPO<sub>4</sub>F<sub>1-x</sub>O<sub>x</sub> Tavorite-Type Compositions: Influence of the Concentration of Vanadyl-Type Defects on the Structure and Electrochemical Performance. *Chem. Mater.* **2018**, *30* (16), 5682–5693. <https://doi.org/10.1021/acs.chemmater.8b02138>.
- (10) Nguyen, L. H. B.; Broux, T.; Camacho, P. S.; Denux, D.; Bourgeois, L.; Belin, S.; Iadecola, A.; Fauth, F.; Carlier, D.; Olchowka, J.; Masquelier, C.; Croguennec, L. Stability in Water and Electrochemical Properties of the Na<sub>3</sub>V<sub>2</sub>(PO<sub>4</sub>)<sub>2</sub>F<sub>3</sub> – Na<sub>3</sub>(VO)<sub>2</sub>(PO<sub>4</sub>)<sub>2</sub>F Solid Solution. *Energy Storage Materials* **2019**, *20*, 324–334. <https://doi.org/10.1016/j.ensm.2019.04.010>.
- (11) Ellis, B. L.; Nazar, L. F. Anion-Induced Solid Solution Electrochemical Behavior in Iron Tavorite Phosphates. *Chem. Mater.* **2012**, *24* (6), 966–968. <https://doi.org/10.1021/cm203543q>.
- (12) Boivin, E.; Chotard, J.-N.; Masquelier, C.; Croguennec, L. Towards Reversible High-Voltage Multi-Electron Reactions in Alkali-Ion Batteries Using Vanadium Phosphate Positive Electrode Materials. *Molecules* **2021**, *26* (5), 1428. <https://doi.org/10.3390/molecules26051428>.
- (13) Boivin, E.; Chotard, J.-N.; Ménétrier, M.; Bourgeois, L.; Bamine, T.; Carlier, D.; Fauth, F.; Masquelier, C.; Croguennec, L. Oxidation under Air of Tavorite LiVPO<sub>4</sub>F: Influence of Vanadyl-Type Defects on Its Electrochemical Properties. *J. Phys. Chem. C* **2016**, *120* (46), 26187–26198. <https://doi.org/10.1021/acs.jpcc.6b07342>.
- (14) Serras, P.; Palomares, V.; Alonso, J.; Sharma, N.; López del Amo, J. M.; Kubiak, P.; Fdez-Gubieda, M. L.; Rojo, T. Electrochemical Na Extraction/Insertion of Na<sub>3</sub>V<sub>2</sub>O<sub>2x</sub>(PO<sub>4</sub>)<sub>2</sub>F<sub>3-2x</sub>. *Chem. Mater.* **2013**, *25* (24), 4917–4925. <https://doi.org/10.1021/cm403679b>.
- (15) Serras, P.; Palomares, V.; Goñi, A.; Gil de Muro, I.; Kubiak, P.; Lezama, L.; Rojo, T. High Voltage Cathode Materials for Na-Ion Batteries of General Formula Na<sub>3</sub>V<sub>2</sub>O<sub>2x</sub>(PO<sub>4</sub>)<sub>2</sub>F<sub>3-2x</sub>. *J. Mater. Chem.* **2012**, *22* (41), 22301. <https://doi.org/10.1039/c2jm35293a>.
- (16) Park, Y.-U.; Seo, D.-H.; Kim, H.; Kim, J.; Lee, S.; Kim, B.; Kang, K. A Family of High-Performance Cathode Materials for Na-Ion Batteries, Na<sub>3</sub>(VO<sub>1-x</sub>PO<sub>4</sub>)<sub>2</sub>F<sub>1+2x</sub> (0 ≤ x ≤ 1): Combined First-Principles and Experimental Study. *Adv. Funct. Mater.* **2014**, *24* (29), 4603–4614. <https://doi.org/10.1002/adfm.201400561>.
- (17) Kim, H.; Seo, D.-H.; Bianchini, M.; Clément, R. J.; Kim, H.; Kim, J. C.; Tian, Y.; Shi, T.; Yoon, W.-S.; Ceder, G. A New Strategy for High-Voltage Cathodes for K-Ion Batteries: Stoichiometric KVPO<sub>4</sub>F. *Adv. Energy Mater.* **2018**, *8* (26), 1801591. <https://doi.org/10.1002/aenm.201801591>.
- (18) Petříček, V.; Dušek, M.; Palatinus, L. Crystallographic Computing System JANA2006: General Features. *Zeitschrift für Kristallographie - Crystalline Materials* **2014**, *229* (5). <https://doi.org/10.1515/zkri-2014-1737>.
- (19) Bérar, J.-F.; Lelann, P. E.s.d.'s and Estimated Probable Error Obtained in Rietveld Refinements with Local Correlations. *Journal of Applied Crystallography* **1991**, *24* (1), 1–5. <https://doi.org/10.1107/S0021889890008391>.
- (20) Momma, K.; Izumi, F. VESTA: A Three-Dimensional Visualization System for Crystallographic and Structural Analysis. *J Appl Crystallogr* **2008**, *41* (3), 653–658. <https://doi.org/10.1107/S0021889808012016>.
- (21) Briois, V.; La Fontaine, C.; Belin, S.; Barthe, L.; Moreno, T.; Pinty, V.; Carcy, A.; Girardot, R.; Fonda, E. ROCK: The New Quick-EXAFS Beamline at SOLEIL. *J. Phys.: Conf. Ser.* **2016**, *712*, 012149. <https://doi.org/10.1088/1742-6596/712/1/012149>.
- (22) Ravel, B.; Newville, M. ATHENA, ARTEMIS, HEPHAESTUS: Data Analysis for X-Ray Absorption Spectroscopy Using IFEFFIT. *J Synchrotron Rad* **2005**, *12* (4), 537–541. <https://doi.org/10.1107/S0909049505012719>.
- (23) Sahlé, Ch. J.; Mirone, A.; Niskanen, J.; Inkinen, J.; Krisch, M.; Huotari, S. Planning, Performing and Analyzing X-Ray Raman Scattering Experiments. *J Synchrotron Rad* **2015**, *22* (2), 400–409. <https://doi.org/10.1107/S1600577514027581>.
- (24) Kresse, G.; Joubert, D. From Ultrasoft Pseudopotentials to the Projector Augmented-Wave Method. *Physical Review B* **1999**, *59* (3), 1758–1775. <https://doi.org/10.1103/PhysRevB.59.1758>.
- (25) Blöchl, P. E. Projector Augmented-Wave Method. *Physical Review B* **1994**, *50* (24), 17953–17979. <https://doi.org/10.1103/PhysRevB.50.17953>.
- (26) Kresse, G.; Hafner, J. Ab Initio Molecular Dynamics for Liquid Metals. *Physical Review B* **1993**, *47* (1), 558–561. <https://doi.org/10.1103/PhysRevB.47.558>.
- (27) Kresse, G.; Furthmüller, J. Efficiency of Ab-Initio Total Energy Calculations for Metals and Semiconductors Using a Plane-Wave Basis Set. *Computational Materials Science* **1996**, *6* (1), 15–50. [https://doi.org/10.1016/0927-0256\(96\)00008-0](https://doi.org/10.1016/0927-0256(96)00008-0).
- (28) Kresse, G.; Hafner, J. Ab Initio Molecular-Dynamics Simulation of the Liquid-Metalamorphous- Semiconductor Transition in Germanium. *Physical Review B* **1994**, *49* (20), 14251–14269. <https://doi.org/10.1103/PhysRevB.49.14251>.
- (29) Kresse, G.; Furthmüller, J. Efficient Iterative Schemes for Ab Initio Total-Energy Calculations Using a Plane-Wave Basis Set. *Physical Review B - Condensed Matter and Materials Physics* **1996**, *54* (16), 11169–11186. <https://doi.org/10.1103/PhysRevB.54.11169>.
- (30) Perdew, J. P.; Burke, K.; Ernzerhof, M. Generalized Gradient Approximation Made Simple. *Physical Review Letters* **1996**, *77* (18), 3865–3868. <https://doi.org/10.1103/PhysRevLett.77.3865>.
- (31) Dudarev, S.; Botton, G. Electron-Energy-Loss Spectra and the Structural Stability of Nickel Oxide: An LSDA+U Study. *Physical Review B - Condensed Matter and Materials Physics* **1998**, pp 1505–1509. <https://doi.org/10.1103/PhysRevB.57.1505>.
- (32) Castets, A.; Carlier, D.; Zhang, Y.; Boucher, F.; Marx, N.; Croguennec, L.; Ménétrier, M. Multinuclear NMR and DFT Calculations on the LiFePO<sub>4</sub>-OH and FePO<sub>4</sub>-H<sub>2</sub>O Homeotypic Phases. *The Journal of Physical Chemistry C* **2011**, *115* (32), 16234–16241. <https://doi.org/10.1021/jp204767c>.
- (33) Castets, A.; Carlier, D.; Zhang, Y.; Boucher, F.; Ménétrier, M. A DFT-Based Analysis of the NMR Fermi Contact Shifts in Tavorite-like LiMPO 4-OH and MPO 4-H<sub>2</sub>O (M = Fe, Mn, V). *Journal of Physical Chemistry C* **2012**, *116* (34), 18002–18014. <https://doi.org/10.1021/jp302549s>.
- (34) Bamine, T.; Boivin, E.; Boucher, F.; Messinger, R. J.; Salager, E.; Deschamps, M.; Masquelier, C.; Croguennec, L.; Ménétrier, M.; Carlier, D. Understanding Local Defects in Li-Ion Battery Electrodes through Combined DFT/NMR Studies: Application to LiVPO<sub>4</sub>F. *Journal of Physical Chemistry C* **2017**, *121* (6), 3219–3227. <https://doi.org/10.1021/acs.jpcc.6b11747>.
- (35) Nguyen, L. H. B.; Sanz Camacho, P.; Broux, T.; Olchowka, J.; Masquelier, C.; Croguennec, L.; Carlier, D. Density Functional Theory-Assisted 31 P and 23 Na Magic-Angle Spinning Nuclear Magnetic Resonance Study of the Na<sub>3</sub>V<sub>2</sub>(PO<sub>4</sub>)<sub>2</sub>F<sub>3</sub>–Na<sub>3</sub>V<sub>2</sub>(PO<sub>4</sub>)<sub>2</sub>FO<sub>2</sub> Solid Solution: Unraveling Its Local and Electronic Structures. *Chemistry of Materials* **2019**, *31* (23), 9759–9768. <https://doi.org/10.1021/acs.chemmater.9b03546>.
- (36) Mukharjee, P. K.; Somesh, K.; Ranjith, K. M.; Baenitz, M.; Skourski, Y.; Adroja, D. T.; Khalyavin, D.; Tsirlin, A. A.; Nath, R. Quantum Magnetism of Ferromagnetic Spin Dimers in α-KVPO 4. *Phys. Rev. B* **2021**, *104* (22), 224409. <https://doi.org/10.1103/PhysRevB.104.224409>.
- (37) Evans, J. C. The Vibrational Spectra and Structure of the Vanadyl Ion in Aqueous Solution. *Inorg. Chem.* **1963**, *2* (2), 372–375. <https://doi.org/10.1021/ic50006a031>.
- (38) Schindler, M.; Hawthorne, F. C.; Baur, W. H. Crystal Chemical Aspects of Vanadium: Polyhedral Geometries, Characteristic Bond Valences, and Polymerization of (VO<sub>n</sub>) Polyhedra. *Chem. Mater.* **2000**, *12* (5), 1248–1259. <https://doi.org/10.1021/cm990490y>.
- (39) de Groot, F.; Vankó, G.; Glatzel, P. The 1s X-Ray Absorption Pre-Edge Structures in Transition Metal Oxides. *J. Phys.: Condens. Matter* **2009**, *21* (10), 104207. <https://doi.org/10.1088/0953-8984/21/10/104207>.
- (40) Wong, J.; Lytle, F. W.; Messmer, R. P.; Maylotte, D. H. K-Edge Absorption Spectra of Selected Vanadium Compounds. *Phys. Rev. B* **1984**, *30* (10), 5596–5610. <https://doi.org/10.1103/PhysRevB.30.5596>.
- (41) Chaurand, P.; Rose, J.; Briois, V.; Salome, M.; Proux, O.; Nassif, V.; Olivi, L.; Susini, J.; Hazemann, J.-L.; Bottero, J.-Y. New Methodological Approach for the Vanadium K-Edge X-Ray Absorption Near-Edge Structure Interpretation: Application to the Speciation of Vanadium in Oxide Phases from Steel Slag. *J. Phys. Chem. B* **2007**, *111* (19), 5101–5110. <https://doi.org/10.1021/jp063186i>.
- (42) Retegan, M. *Retegan, Marius, Crispy: V0.7.3, 2019*; Zenodo, 2019. <https://doi.org/10.5281/zenodo.3258065>.

- (43) Haverkort, M. W.; Zwierzycki, M.; Andersen, O. K. Multiplet Ligand-Field Theory Using Wannier Orbitals. *Phys. Rev. B* **2012**, *85* (16), 165113. <https://doi.org/10.1103/PhysRevB.85.165113>.
- (44) Caracciolo, L.; Madec, L.; Petit, E.; Gabaudan, V.; Carlier, D.; Croguennec, L.; Martinez, H. Electrochemical Redox Processes Involved in Carbon-Coated KVPO<sub>4</sub>F for High Voltage K-Ion Batteries Revealed by XPS Analysis. *J. Electrochem. Soc.* **2020**, *167* (13), 130527. <https://doi.org/10.1149/1945-7111/abb0c>.
- (45) Boivin, E.; Iadecola, A.; Fauth, F.; Chotard, J.-N.; Masquelier, C.; Croguennec, L. Redox Paradox of Vanadium in Tavorite LiVPO<sub>4</sub>F<sub>1-y</sub>O<sub>y</sub>. *Chem. Mater.* **2019**, *31* (18), 7367–7376. <https://doi.org/10.1021/acs.chemmater.9b01987>.
- (46) Castets, A.; Carlier, D.; Trad, K.; Delmas, C.; Ménétrier, M. Analysis of the 7 Li NMR Signals in the Monoclinic Li<sub>3</sub>Fe<sub>2</sub>(PO<sub>4</sub>)<sub>3</sub> and Li<sub>3</sub>V<sub>2</sub>(PO<sub>4</sub>)<sub>3</sub> Phases. *The Journal of Physical Chemistry C* **2010**, *114* (44), 19141–19150. <https://doi.org/10.1021/jp106871z>.
- (47) Carlier, D.; Ménétrier, M.; Delmas, C. Transferred Hyperfine Interaction between a Tetrahedral Transition Metal and Tetrahedral Lithium: Li<sub>6</sub>CoO<sub>4</sub>. *Journal of Physical Chemistry C* **2010**, *114* (10), 4749–4755. <https://doi.org/10.1021/jp911364w>.
- (48) Ballhausen, C. J.; Gray, H. B. The Electronic Structure of the Vanadyl Ion. *Inorg. Chem.* **1962**, *1* (1), 111–122. <https://doi.org/10.1021/ic50001a022>.
- (49) Lian, R.; Wang, D.; Ming, X.; Zhang, R.; Wei, Y.; Feng, J.; Meng, X.; Chen, G. Phase Transformation, Ionic Diffusion, and Charge Transfer Mechanisms of KVOPO<sub>4</sub> in Potassium Ion Batteries: First-Principles Calculations. *J. Mater. Chem. A* **2018**, *6* (33), 16228–16234. <https://doi.org/10.1039/C8TA06708B>.

---

TABLE OF CONTENT FIGURE

